

Provided by the author(s) and University of Galway in accordance with publisher policies. Please cite the published version when available.

Title	A dislocation-based model for high temperature cyclic viscoplasticity of 9-12Cr steels
Author(s)	Barrett, Richard A.; O'Donoghue, Peter E.; Leen, Sean B.
Publication Date	2015-06-22
Publication Information	Barrett, RA, O Donoghue, PE, Leen, SB (2015) 'A dislocation-based model for high temperature cyclic viscoplasticity of 9-12Cr steels'. Journal Of Pressure Vessel Technology, .
Publisher	Elsevier ScienceDirect
Link to publisher's version	http://dx.doi.org/10.1016/j.commatsci.2014.05.034
Item record	http://hdl.handle.net/10379/5459

Downloaded 2024-04-17T11:55:06Z

Some rights reserved. For more information, please see the item record link above.



A dislocation-based model for high temperature cyclic viscoplasticity of 9-12Cr steels

R.A. Barrett^{1,2,*}, P.E. O'Donoghue^{2,3}, S.B. Leen^{1,2}

¹Mechanical Engineering, College of Engineering and Informatics, NUI Galway, Ireland

²Ryan Institute for Environmental, Marine and Energy Research, NUI Galway, Ireland

³Civil Engineering, College of Engineering and Informatics, NUI Galway, Ireland

Abstract: A dislocation-based model for high temperature cyclic viscoplasticity in 9-12Cr steels is presented. This model incorporates (i) cyclic softening via decrease in overall dislocation density, loss of low angle boundary dislocations and coarsening of the microstructure and (ii) kinematic hardening via precipitate strengthening and dislocation substructure hardening. The effects of the primary microstructural variables, viz. precipitate radii, dislocation density and martensitic lath width on cyclic viscoplasticity, reveal a size effect of initial precipitate radii and volume fraction, with smaller radii and a higher density of precipitate producing a stronger material. A similar effect is also predicted for initial martensitic lath width at temperatures below 500 °C. The model is intended for microstructure sensitive design of high temperature materials and components for next generation power plant technology.

1. Introduction

Modern power generation plants operating under subcritical conditions are subjected to significant and increasingly more frequent thermal gradients due to the current shift from base-load (constant load) to load-following (intermittent-mode) operation. This change is driven by (i) a requirement to reduce emissions from fossil fuel plant, (ii) the control of energy cost by continuous mixing of energy sources and (iii) the intermittent nature of renewable energy. The complex operational cycles [1, 2] which current and future plant must endure, therefore, leads to thermo-mechanical fatigue (TMF) and creep-fatigue (CF) failure. These failures commonly occur within the heat affected zone (HAZ) of welded connections (Type IV cracking) [3], sometimes as early as 5-10% of the plant design life. Coupled with the need for more corrosion resistant materials to withstand biomass co-firing, the global strategic goal of ultra-supercritical (USC) plant operation (e.g. steam pressure increased from 16 MPa to 27 MPa [4] and steam temperature to increase beyond 600 °C) to significantly increase overall plant efficiency and reduce emissions will require (i) characterisation of the current generation of power plant materials under flexible loading conditions and (ii) an improved family of materials with the capability to withstand high temperature fatigue and creep loading conditions and increased steam corrosion.

The present work, as a starting point, is predicated on multi-scale modelling of the current state of the art USC candidate materials, viz. 9-12Cr martensitic steels. The high strength of such materials is achieved by a martensitic lath-based microstructure which is tempered to produce a nano-scale precipitate strengthened material. Due to the complex nature of the evolution of the microstructure of 9-12Cr steels [5, 6], a multi-scale modelling approach is required. One of the key requirements for

* Corresponding Author:
Email: r.barrett2@nuigalway.ie
Tel: +353 91 493020
Fax: +353 91 563991

such an approach is the development of a macro-scale material model based on the key microstructural variables of dislocation density, martensitic lath structure and the various precipitates.

Currently, a range of phenomenological material models exist for high temperature fatigue, including the Chaboche unified power law [7-10], the two-layer viscoplasticity model [1, 2] and more recently, the authors have developed a hyperbolic sine unified formulation [11-13] which enables reliable extrapolation from strain-rates at which experiments are conducted to strain-rates typically observed in plant (Fig. 1). However, these approaches are limited with respect to prediction of micro-structurally driven phenomena, in particular, cyclic softening [14, 15], but also kinematic hardening, which are key to material and plant integrity. To capture the material behaviour across a wider range of loading conditions, a modelling approach based on the physical mechanisms of deformation will give more accurate extrapolation and interpolation, and hence, life prediction.

A number of material models based on the physical mechanisms of creep have been developed [16-19] and applied to 9-12Cr steels [20-26]. Material models, e.g. [27], have also been developed to capture specific mechanisms of deformation under cyclic loading, such as the dislocation network evolution. Strain gradient crystal plasticity (CP) material models [28-32] have been employed to obtain a back-stress for the Bauschinger effect through the inclusion of geometrically necessary dislocations (GNDs) within a crystal plasticity UEL user subroutine, as well as the presence of carbides geometrically in the finite element (FE) model. Sauzay et al. [14, 15, 33] have presented a physically-based model for cyclic softening of 9-12Cr steels. However, to date, no corresponding model based on the physical mechanisms of the Bauschinger effect and kinematic hardening has been developed.

Thus, this paper presents a macro-scale constitutive model which enables a more mechanistic and efficient approach to modelling kinematic hardening, via a back-stress, dependent on the primary strengthening mechanisms of 9-12Cr steels, coupled with appropriate models to describe the evolution of the primary strengthening variables under cyclic loading conditions. A dislocation-based model for cyclic softening is also developed here based on the key micromechanical phenomena, e.g. loss of dislocations at low angle boundaries (LABs). The model thus incorporates the mean effects of the key micro-structural parameters to enable more reliable extrapolation and interpolation across a broad range of loading conditions. It is anticipated that this approach will help to predict key failure and life-limiting behaviour, such as Type IV cracking in plant components [34]. The new material model is applied to high temperature cyclic plasticity experiments conducted on an ex-service P91 steel.

2. Microstructure of 9-12Cr steels

2.1. Heat treatment and hierarchical microstructure

The microstructure of 9-12Cr steels is a typical tempered martensitic structure shown schematically in Fig. 2. This hierarchical microstructure consists of prior austenite grains (PAGs), packets and blocks, all of which are high-angle boundaries with an angle of misorientation greater than 5° . Blocks are subdivided into martensitic laths, defined as low-angle boundary (LAB) regions with similar angles of misorientation less than 5° . This matrix structure is further strengthened by various precipitates and solutes, which are described in more detail below. Typical dimensions for the PAGs are approximately 100 μm , blocks are approximately 4 μm [15] and the width of the martensitic laths are of the order of 0.37-0.7 μm [6, 15]. This complex microstructure forms due to the heat treatment of 9-12Cr steels, as illustrated schematically in Fig. 3. The material is firstly normalised for a period of up to 2 hrs at temperatures of approximately 1100 $^\circ\text{C}$, resulting in an austenite structure. The material is

then cooled rapidly to produce a martensitic transformation with a lath martensite structure and an extremely high dislocation density. A tempering process at around 750 °C for 1 to 2 hrs is then applied to improve ductility. Tempering results in the formation of the various precipitates [5, 35] and also partly reduces the overall dislocation density. The specific heat treatment of the P91 steel discussed here, which was fabricated via a rolling process, was normalisation at 1050 °C for 0.5 hr, followed by tempering at 765 °C for 1 hr [36].

2.2. Strengthening mechanisms in 9-12Cr steels

The main strengthening mechanisms of 9-12Cr steels are produced by the complex matrix microstructure described above, coupled with the presence of several solutes and precipitates in the material, as highlighted in Fig. 4. Dislocation strengthening is obtained via (i) dislocation-dislocation interactions in which mobile dislocations become tangled with immobile dislocations in the lath interiors, (ii) work hardening due to the presence of immobile dislocations which trap mobile dislocations, and (iii) the production of dislocation pile-ups at HABs (grain boundary strengthening). For 9-12Cr steels, two main solutes are present, namely the Mo and W solutes. These solutes exert work hardening by providing a pinning mechanism which retards the motion of mobile dislocations and hence, reduces plastic deformation. The final strengthening mechanism is due to the presence of precipitates, both within the lath interiors and along boundaries. Assuming that the mean precipitate radius in the tempered microstructure is too large for particle shearing to occur, mobile dislocations form Orowan loops around the precipitates, resulting in the given mobile dislocation becoming immobile as illustrated in Fig. 5. There are several types of precipitate present in 9-12Cr steels. In the 'as-received' material, two main categories of precipitate exist, i.e. the $M_{23}C_6$ and MX precipitates. The $M_{23}C_6$ carbonitrides, where $M=Fe, Cr, \text{ or } Mo$, are typically dispersed along boundaries [6, 37-41]. In the lath interiors, smaller MX precipitates are formed during the tempering process and can be divided into two types, namely VN and NbC precipitates, both of which provide a pinning mechanism within lath interiors.

High temperature loading causes temperature-dependent coarsening of the precipitates, which virtually diminishes at temperatures below 550 °C [42] and long-term high temperature loading also results in the precipitation of two new secondary phase particles. The first of these are Laves phase precipitates, which consume the Mo and W solutes to form Fe_2Mo and Fe_2W particles respectively and the second are Z-phase particles. As precipitation of these new phases is a long-term effect, their formation and associated microstructural degradation are not explicitly modelled here.

2.3. Cyclic softening

One of the key contributions to a loss of strength in 9-12Cr steels under fatigue, TMF and CF loading conditions is cyclic softening [14], which typically occurs in materials with a high initial dislocation density. The significant measured effects of cyclic softening on the material stress-strain response is illustrated in Fig. 6 for the P91 steel of the present study [36]. The work of Sauzay and co-workers [14, 15, 33], concluded that the physical mechanisms behind cyclic softening in 9-12Cr steels are: (i) a loss in overall dislocation density, (ii) a loss of the LAB dislocations eventually resulting in a disappearance of the LAB and a decrease in the angle of misorientation between LABs, (iii) a subsequent coarsening of the martensitic lath microstructure and (iv) precipitate coarsening at higher temperatures. Due to the presence of $M_{23}C_6$ precipitates along boundaries, it is assumed that HABs (PAGs, packets and blocks) do not coarsen due to cyclic deformation. Coarsening of LABs is attributed here to the mechanism of LAB annihilation in which the angle of misorientation reduces to zero. As Sauzay and co-workers [15] have illustrated for lath coarsening, the $M_{23}C_6$ precipitates, which were originally present on LABs, remain behind after the LAB has disappeared and form part of the coarsened lath interior.

3. Dislocation-based material model

The material model is defined in terms of a number of micro-structural variables describing the main strengthening and cyclic softening mechanisms, within a hyperbolic sine flow rule framework [11]. The increment in stress, $\Delta\sigma$, is defined using Hooke's law:

$$\Delta\sigma = E\Delta\varepsilon^{\text{el}} = E(\Delta\varepsilon - \Delta\varepsilon^{\text{pl}}) \quad (1)$$

where E is Young's modulus and $\Delta\varepsilon^{\text{el}}$, $\Delta\varepsilon$ and $\Delta\varepsilon^{\text{pl}}$ are the increments in elastic, total and plastic strain, respectively. To enable more accurate extrapolation from the strain-rates conducted in laboratory experiments to the strain-rates typically observed in realistic plant [11, 13, 43], a hyperbolic sine material model is used to simulate strain-rate sensitivity and strain-rate independence of the material parameters. Thus, the flow rule for the increment in plastic strain is defined using the following equation set:

$$\dot{\varepsilon}^{\text{pl}} = \alpha \sinh \beta f \operatorname{sgn}(\sigma - \sigma_b) \quad (2)$$

$$f = |\sigma - \sigma_b| - \sigma_y^{\text{cyc}} \quad (2)$$

$$\dot{p} = |\dot{\varepsilon}^{\text{pl}}|$$

where f is the viscous stress for $f > 0$ and defines the elastic domain for $f \leq 0$, \dot{p} is the accumulated effective plastic strain-rate, α and β are the cyclic viscoplastic material parameters, σ is stress, σ_b is the back-stress, which accounts for the strengthening mechanisms in 9-12Cr steels, and σ_y^{cyc} is the cyclic yield stress, which accounts for the dislocation-based cyclic softening. The main strengthening mechanisms represented in the present model are: (i) Mo (and W for P92 steels) solute strengthening mechanisms, σ_{sol} , (ii) precipitate strengthening, σ_p , and (iii) martensitic lath hardening coupled with a back-stress produced by the presence of the dislocation network within a hierarchical grain structure, σ_d . For monotonic loading, the back-stress is defined using a linear superposition of the above mentioned strengthening mechanisms. However, for fully reversed loading, the deformation is capable of overcoming the stresses produced by the solutes and dislocation network. It is also assumed that the presence of the precipitates facilitates the deformation process during reverse loading [44]. Thus, the hardening rate is assumed to be independent of dislocation density evolution during reverse loading and the back-stress is defined as:

$$\dot{\sigma}_b = \begin{cases} \dot{\sigma}_{\text{sol}} + \dot{\sigma}_p + \dot{\sigma}_d & \text{monotonic loading} \\ 2\dot{\sigma}_p & \text{fully reversed} \end{cases} \quad (3)$$

where σ_{sol} , σ_p and σ_d are the back-stresses produced by solute strengthening, precipitate hardening and a dislocation substructure respectively. For long-term creep, a solute strengthening model such as [45, 46], which accounts for multiple solutes (e.g. Mo and W in 9-12Cr steels) is required. However, due to the short-term nature of the present application, the evolution of the σ_{sol} back-stress with time can be assumed to be negligible. The evolution of cyclic yield stress, σ_y^{cyc} , is based on the cyclic evolution of dislocation density, ρ , where the cyclic yield stress is defined as:

$$\sigma_y^{\text{cyc}} = \sigma_{\text{PN}} + \alpha_1 M G b \sqrt{\rho} \quad (4)$$

where σ_{PN} is the Peierls-Nabarro stress, α_1 is a material parameter, M is the Taylor factor, G is the shear modulus and b is the magnitude of the Burgers vector. The time evolution of the cyclic yield stress is thus:

$$\dot{\sigma}_y^{cyc} = \frac{\alpha_1 M G b}{2\sqrt{\rho}} \dot{\rho} \quad (5)$$

σ_{PN} does not evolve as a function of time here and temperature dependence of the yield stress is accounted for via the temperature dependent shear modulus, G . The above material model is implemented in uniaxial form within a standalone computer program. A flowchart of the main processes in this implementation is presented in Fig. 7.

3.1. Precipitate hardening

The Fisher-Hart-Pry (FHP) model [47, 48] is used to simulate the back-stress caused by the presence of the various precipitates. For small strain monotonic loading and a single precipitate of type j , the precipitate hardening produced is:

$$\sigma_p = \sigma_0 \left[1 + 6 \left(\frac{CG}{\sigma_0} \right)^{1/2} f_j^{3/4} \sqrt{p} + 18 \frac{CG}{\sigma_0} f_j^{3/2} p \right] \quad (6)$$

In equation (6), σ_0 is the Orowan stress, f_j is the volume fraction of precipitate type j and C is a material parameter, defined as [48]:

$$C = 0.509 \left[1 + \frac{\nu}{2(1-\nu)} \right] \quad (7)$$

where ν is Poisson's ratio. Thus, differentiating equation (6) with respect to time and adapting the FHP model for cyclic plasticity, the evolution of hardening due to m precipitates is defined as:

$$\dot{\sigma}_p = \sum_{j=1}^m \left[3(\sigma_{0,j} CG)^{1/2} f_j^{3/4} \frac{1}{\sqrt{p^{cyc}}} + 18 CG f_j^{3/2} \right] \dot{p} \operatorname{sgn}(\sigma - \sigma_b) \quad (8)$$

where p^{cyc} is the cyclic range of effective plastic strain accumulated during load reversal. The Orowan stress associated with a precipitate of type j is defined as:

$$\sigma_{0,j} = \frac{M G b}{\lambda_j} \quad (9)$$

where λ_j is the inter-particle spacing, defined as [24]:

$$\lambda_j = \frac{r_j}{\sqrt{6f_j/\pi}} - 2r_j \sqrt{\frac{2}{3}} \quad (10)$$

with r_j as the mean precipitate radius. In the present study, it is assumed that insignificant particle coarsening occurs during high temperature cyclic plasticity, i.e. r_j is assumed to be constant.

3.2. Dislocation strengthening and evolution of dislocation density

Dislocation-based work hardening occurs as mobile dislocations interact with immobile dislocations in lath interiors and at lath boundaries. Thus, the contribution to the flow stress from the dislocation network using the approach of [19, 49], extended to the continuum level using the Taylor factor, is defined as:

$$\sigma_d = \alpha_1 M G b \sqrt{\rho_i} + \alpha_2 M G b \left(\frac{1}{\delta} + \frac{1}{D} \right) \quad (11)$$

where ρ_i is the lath interior immobile dislocation density, α_2 is a material parameter, δ is the martensitic lath width and D is PAG size. Assuming that PAGs do not coarsen during short-term cyclic plasticity, the hardening rate due to the dislocation structure is defined as:

$$\dot{\sigma}_d = M G b \left(\alpha_1 \frac{\dot{\rho}_i}{\sqrt{\rho_i}} - \alpha_2 \frac{\dot{\delta}}{\delta^2} \right) \quad (12)$$

The evolution of dislocation density is defined here in three distinct groups (as illustrated in Fig. 4): (i) mobile dislocations, ρ_m , (ii) lath interior immobile dislocations, ρ_i , and (iii) lath boundary immobile dislocations, ρ_w , so that the overall dislocation density, ρ , is defined as:

$$\rho = \rho_m + (1 - f_w) \rho_i + f_w \rho_w \quad (13)$$

where f_w is the volume fraction of the lath boundary regions. As mobile dislocations are the carriers of plastic deformation, the Orowan equation [50] is used to define mobile dislocation density evolution rate in terms of the rate of deformation:

$$\dot{\rho}_m = \frac{\dot{\gamma}^{pl}}{b L_e} \quad (14)$$

where $\dot{\gamma}^{pl}$ is the crystallographic plastic slip-rate and L_e is the mean free path travelled by a mobile dislocation before it is annihilated or immobilised. To relate the microscopic plastic slip-rate, $\dot{\gamma}^{pl}$, to the macroscopic plastic strain-rate, $\dot{\epsilon}^{pl}$, the Taylor model is used [51]:

$$n_s \dot{\gamma}^{pl} = M \dot{p} \quad (15)$$

where n_s is the number of active slip systems required to define the deformation-rate in the Taylor model. In this model, due to the assumption of incompressibility, only five independent components of plastic strain-rate are required to define the deformation of a polycrystal material. Hence, the combination of deformation-rates from five slip systems which contribute the lowest energy dissipation must be identified using Taylor's minimum work principle. However, as the macroscale model presented here is independent of slip system, i.e. the level of deformation per slip system is homogeneous across all slip systems, the contribution of five active slip systems (of 48 active slip systems for BCC) will suffice to define the deformation-rate and following the work of [33], n_s is assigned a constant value of 5.

The evolution of mobile dislocation density includes both growth and consumption terms, where the growth of mobile dislocations is determined using the Orowan equation above. Following the work of Cheong and Busso [28, 29], the probability of a mobile dislocation consumption event occurring is $P=0.5A\rho_m$, where A is the critical area for consumption of mobile dislocations. The present study extends the approach of [28, 29] to the macro-scale and includes consumption of mobile dislocations via the mechanisms discussed in [17]; namely (i) mutual annihilation of two mobile dislocations, (ii) the formation of immobile locked configurations and (iii) dipole dislocation formation, as well as incorporating LAB annihilation as described in [14, 15]. The critical areas for consumption for each event are illustrated schematically in Fig. 8 and the evolution equation for mobile dislocation density is:

$$\dot{\rho}_m = \frac{\dot{p}M}{bn_s} \left(\frac{1}{L_e} - \rho_m (2d_{\text{dip}} + 4d_{\text{lock}}(n_s - 1) + d_e) \right) \quad (16)$$

where d_e , d_{dip} and d_{lock} are the critical distances for loss of mobile dislocations due to annihilation, dipole formation and locked configurations, respectively. The mean free path is defined as:

$$L_e = \frac{\delta}{\kappa} \quad (17)$$

where κ is a material parameter. The evolution of lath interior immobile dislocations accounts for the loss of mobile dislocations due to the formation of immobile locked configurations and the loss of immobile dislocations via climb processes. Thus, the evolution equation is defined as [21, 22]:

$$\dot{\rho}_i = \frac{\dot{p}M}{bn_s} 4d_{\text{lock}}(n_s - 1)\rho_m - m_{\text{cl}}Gb^2\rho_i^2 \quad (18)$$

where m_{cl} is the climb mobility rate of dislocations. From the Taylor hardening equation, $\sigma_w = \alpha_1 M G b \rho_w^{1/2}$, and equation (11), the density of immobile dislocations at lath walls is:

$$\rho_w = \left(\frac{\alpha_2}{\alpha_1} \frac{1}{\delta} \right)^2 \quad (19)$$

with a subsequent rate evolution given by:

$$\dot{\rho}_w = 2 \left(\frac{\alpha_2}{\alpha_1} \right)^2 \frac{\dot{\delta}}{\delta^3} \quad (20)$$

3.3. Evolution of the lath microstructure

The growth of martensitic laths is assumed here to consist of two mechanisms, a static term defining time-dependent growth due to high temperature and a dynamic component accounting for the dependence on applied plastic strain [52]. This model has been adapted to include an Arrhenius temperature-dependent function describing the static grain growth term:

$$\dot{\delta} = \left(\alpha_{\delta,0} \exp \left(\frac{-Q_{\delta}}{\bar{R}T} \right) + \beta_{\delta} \dot{p} \right) \delta^{-\gamma_{\delta}} \quad (21)$$

where γ_{δ} is a material parameter, $\alpha_{\delta,0}$ is a static lath growth model parameter, Q_{δ} is the activation energy for lath growth, \bar{R} is the universal gas constant and β_{δ} is a dynamic lath growth material parameter.

4. Results

4.1. Parameter identification

The ex-service P91 steel of the present study has been subjected to 35,168 hrs service under subcritical loading conditions, with 65 start-up cycles. The chemical composition of this material prior to industrial service is shown in Table 1 and Fig. 9 is a flowchart illustrating the calibration process for parameter identification. The material parameters within this study may be split into three distinct groups, namely: (i) elastic material parameters, viz. Young's modulus, E , shear modulus, G , Poisson's ratio, ν , and initial yield stress, $\sigma_{y,0}$, (ii) the cyclic viscoplasticity material parameters, α and β , and (iii)

the microstructural material parameters, related to the evolution of dislocation density, coarsening of the lath structure and precipitate hardening.

The elastic material parameters are easily identified from monotonic test data and are presented in Table 2. Although Poisson's ratio is a temperature dependent parameter, for simplicity a constant value of 0.3 is used throughout the present study. The cyclic viscoplasticity material parameters, α and β , are obtained from stress relaxation data as described in [11]. The identified cyclic elasto-viscoplastic material parameters for temperatures of 400 °C, 500°C and 600°C are presented in Table 2.

As 9-12Cr steels are BCC crystals, the magnitude of Burgers vector is 0.248 nm and the Taylor factor is 2.9. The specific microstructural material parameters related to (i) precipitates, (ii) dislocation densities and (iii) evolution of the martensitic laths are defined below. The microstructural material constants employed here are listed in Table 3. The initial mean radii for the $M_{23}C_6$, VN and NbC precipitates have been obtained from measurements using TEM [41]. Similarly the initial volume fractions of a given precipitate were estimated using thermo-kinetic simulations calibrated against experimental data [53].

From the heat treatment process, 9-12Cr steels have an initially high overall dislocation density, with a range of values from $1.6 \times 10^{14} \text{ m}^{-2}$ to $7.5 \times 10^{14} \text{ m}^{-2}$ identified using TEM, e.g. see [15, 54]. To identify an initial value within this range for the P91 steel presented here, the cyclic softening material parameter α_1 and the initial dislocation density, ρ_0 , are identified from the measured initial yield stress across the range of temperatures by rearranging equation (4). The calibrated results are presented in Fig. 10, where α_1 is found to lie within the range 0.2 to 0.4 and ρ_0 within the range mentioned above. The overall dislocation density of the 'as-received' material is approximately 10% greater than that at the lath walls [55], such that the initial lath boundary immobile dislocation density, $\rho_{w,0}$, is $0.9\rho_0$. The initial lath interior immobile dislocation density is assigned a low value of $1 \times 10^{11} \text{ m}^{-2}$ [21]. The critical distance for a dipole dislocation to form is assigned a value of $7b$. The volume fraction at the lath boundaries is defined as [56]:

$$f_w = 1 - \left(1 - \frac{t_w}{\delta}\right)^3 \approx \frac{3t_w}{\delta} \quad (22)$$

where t_w is the cell wall thickness and is assigned a constant value of $100b$ [21]. To account for the effect of the Mo interstitial atoms reducing the climb mobility rate, m_{cl} is defined as [21]:

$$m_{cl} = k_{sol} \frac{D_{Fe} b}{k_b T} \quad (23)$$

where k_{sol} is a solute atom parameter with a value of 0.05 [21], k_b is the Boltzmann constant and D_{Fe} is the diffusion coefficient for iron, defined as:

$$D_{Fe} = D_{Fe,0} e^{-Q_{CR}/RT} \quad (24)$$

where Q_{CR} is the activation energy for creep. The lath material parameters are obtained by fitting the lath evolution model to creep data [57]. Fig. 11 presents the correlation achieved with experimental data during the calibration procedure for the identification of the lath growth parameters $\alpha_{\delta,0}$, β_{δ} and γ_{δ} . The mean size of the prior austenite grains, D , is assigned a constant value of 50 μm .

4.2. Calibration of micro-structural parameters

The material model is calibrated against high temperature cyclic plasticity experiments conducted at a strain-rate of 0.1 %/s [36]. Fig. 12 illustrates the typical correlation achieved with the experimental data for the initial and 600th cycles under the calibration regime at temperatures of 400 °C, 500 °C and 600 °C respectively. From the results of Figs. 12a to 12c, it is evident that the material undergoes significant cyclic softening, which is captured by the model. This ability of the model is verified in Fig. 12d, which compares the maximum stress from the model with the experimental data. Clearly, good agreement with the data is achieved for the calibration conditions of a strain-rate of 0.1 %/s and a strain-range of ± 0.5 %. Table 4 shows the resulting set of micro-structural parameters identified through the calibration process.

4.3. Validation against high temperature cyclic plasticity data

Validation of the performance of the model for extrapolation with respect to strain-rate, for example, is achieved via comparison with high temperature cyclic plasticity data at the alternative strain-rate of 0.025 %/s, across a range of temperatures. Figs. 13a to 13c depict the correlation achieved with the experimental data at temperatures of 400 °C, 500 °C and 600 °C and a strain-rate of 0.025 %/s for the initial and 600th cycles. Fig. 13d demonstrates the capability of the model to predict the softening behaviour of 9-12Cr steels outside the range of calibration. For the 400 °C case, the model captures the material behaviour reasonably well but over predicts cyclic softening. The effect of extrapolating the material model to strain-rates which are more representative of those observed in modern plant is presented in Fig. 14. These results compare the predicted stress-range for strain-rates of 0.1 %/s and 0.0001 %/s respectively. Although the lower strain-rate is still larger than values typically observed in base-load operating plant [58], this result predicts a decrease of 70 MPa in stress-range; this is a significant loss in cyclic strength, e.g. see Fig. 1. This illustrates the need for an ability to accurately extrapolate from laboratory test conditions (typically high) to those observed in realistic loading conditions (typically much lower).

4.4. Effects of micro-structural parameters

The effects of two primary micro-structural variables, namely (i) the initial precipitate radii ($M_{23}C_6$ and MX particles) and (ii) initial lath width, on predicted plastic strain-range is investigated. Five initial precipitate radii, above and below typical values (e.g. see [41]) are considered. Fig 15 illustrates the effect of increasing the initial precipitate radius on the stress-strain response for a stabilised loop. Larger particles result in a weaker material, as the particle spacing is increased, viz. equation (10), assuming constant f_j . For example, increasing r_j from 15 nm to 90 nm causes a 19.5 % reduction in cyclic strength for $M_{23}C_6$ precipitates. Hence, the capability of the pinning mechanism provided by the $M_{23}C_6$ precipitates is significantly reduced. Fig. 16 summaries the results of simulations on the effect of varying the initial precipitate radii. As is evident from Fig. 16, the effect of size of MX precipitates is predicted to be less significant than for $M_{23}C_6$ precipitates.

Fig. 17 shows the effect of initial lath width, δ , on the stress-strain response at 400 °C and 600 °C, respectively, for the 600th cycle, where the initial dislocation density is defined using equation (19). A significant effect of up to 21 % on cyclic strength (stress range) is predicted at the lower temperature of 400 °C. At 600 °C, the effect of stress range and plastic strain range is significantly less for the 600th cycle. Fig. 18 shows the effect of temperature and lath width on the predicted plastic strain-range. Below 500 °C, an intrinsic size effect is predicted, where the presence of more LABs of smaller dimensions inhibits cyclic plasticity and increases cyclic strength. However, at temperatures above 500 °C, initial lath width is predicted to have a negligible effect.

5. Discussion

The model presented simulates the mean effect of precipitate strengthening and dislocation-based hardening. The measured history of hardening has been reasonably well predicted for a range of loading conditions and temperatures, as presented in Fig. 12 for the calibration loading conditions and in Fig. 13 for the validation regime. For monotonic loading, the hardening is a combination of precipitate hardening and immobile dislocation strengthening. However, for fully reversed cyclic loading, where plastic deformation overcomes the dislocation hardening during the monotonic phase, the back-stress produced is primarily dependent on the stress exerted by the presence of the various nano-scale precipitates and their effectiveness in pinning dislocation motion and maintaining a lath hardening structure, e.g. see [59]. The model predicts the effectiveness of smaller precipitate size in increasing the (cyclic) strength and reducing the resultant cyclic plastic strain-range across all temperatures. As Fig 15 illustrates, the effect of the precipitate radius on the predicted stress-strain response is pivotal for the larger and more abundant $M_{23}C_6$ carbonitrides dispersed along LABs, with a minimal size effect observed for the MX precipitates. Fig. 16 shows that a factor of 6.0 increase in $M_{23}C_6$ precipitate size is predicted to cause a 10 % increase in plastic strain-range and 19.5 % decrease in (cyclic) strength. Hence, it is important to ensure that a minimum $M_{23}C_6$ particle radius is achieved during tempering. The effect of a factor of 6 increase in the NbC particles is not as important, giving only a 4 % change in plastic strain-range. It is worth noting that Fig. 16 shows a larger volume fraction effect than particle radius effect as the VN particles, with a higher volume fraction, are predicted to have a greater effect on plastic strain-range than the NbC precipitates.

Fig. 18 indicates an optimum initial lath width of less than 1 μm for the current material. This result is consistent with an intrinsic size effect, i.e. a smaller grain size decreases the predicted plastic strain-range and increases the strength at the lower temperature. Fig. 19 shows the measured effect of strain-rate at 500 °C and 600 °C. There is a negligible effect at 500 °C, but a significant effect at 600 °C. As illustrated in Fig. 18, at the higher temperature, where rate-dependency and creep effects are important, it is predicted that the benefit of smaller lath width is mitigated. This prediction is similar to the findings of Kassener and co-workers [60-62], who have shown experimentally that the flow stress of aluminium alloys under high temperature creep loading is independent of initial subgrain size. However, this effect is attributed here to the lath evolution model (coupled with a strain-rate sensitive constitutive law), which simulates the effects of temperature-induced static lath growth, combined with a lath width size effect. This results in an interaction between (static) lath growth and the lath size effect, such that at higher temperatures, the evolution of lath width overrides (i.e. saturation occurs) the lath size effect after 600 cycles at 600 °C. This is due to the laths coarsening (and saturating) much more rapidly than at 400 °C. Furthermore, the predicted lath width at 600 °C is 3.8 μm after 600 cycles (for $\delta_0 = 0.6 \mu m$), a value which is relatively consistent with the final TEM measured values of 3-4 μm presented in [14] for a P91 steel at a lower temperature of 550 °C. This result at 600 °C also illustrates that the coarsened lath width is approaching the dimension of the HAB blocks (approximately 4 μm and which do not cyclically coarsen). In comparison, a lath width of 1 μm is predicted for the 400 °C case after 600 cycles.

Although the general (qualitative) trends of the latter investigations into the effects of varying the precipitate radii and lath width microstructural parameters can perhaps be deduced from individual equations, the significance of the present work is the quantitative prediction on stress-strain hysteresis (cyclic plasticity) response, which is not possible without solving the complete system of non-linear equations, including the viscoplastic flow-rule equation. The present work forms part of a multi-scale modelling framework for 9-12Cr steels, which will also include simulations using strain-gradient CP at (i) the micro-scale (martensitic lath level) and (ii) meso-scale (block level [63, 64]), for subsequent

quantitative assessment at the component level. Future work will therefore address micro-mechanical prediction of the effects investigated here (cf. Figs 15 to 18), using measured histogram distributions of precipitates and lath widths, for example, as presented by Sweeney et al. [65], for CoCr alloy at room temperature, for example; this will allow significantly smaller-scale assessment of the role of precipitate, lath and block geometries etc. Such detailed micro-mechanical models could then, in principle, be compared with multi-axial user-material FE implementation of the present macro-scale approach to enhance the calibration vis-a-vis the smaller-scale microstructural features. Within this framework, multi-scale life prediction (in particular crack initiation) is also of critical importance. For CP simulations, fatigue indicator parameters (FIPs), e.g. such as the p_{crit} approach of [65, 66] or the minimum energy method of [67], can be used to predict failure. This can, in turn, be mapped up to the macro-scale using polycrystal plasticity theory, e.g. the Taylor model of equation (15), for crack initiation predictions at the macro-scale, to allow micro-structure sensitive life assessment of plant components (under flexible loading). Finally, this will allow plant designers to assess various heat treatments, post-weld heat treatments etc., vis-a-vis optimisation of microstructural parameters such as outlined here. It is anticipated that such this multi-scale methodology will help to solve the problem of Type IV cracking for complex welded (multi-material) connections.

Future work will also explore further enhancements to the current material model, e.g. inclusion of more complex dislocation density evolution models, such as [18], which explicitly simulate both the edge and screw dislocations. Also, the modelling of evolution of the laths will be improved upon by conducting a series of interrupted high temperature cyclic plasticity tests and performing detailed micro-structural analysis on the resulting specimens.

6. Conclusions

The key conclusions of this work are:

- A dislocation-based cyclic softening model is developed to account for the main mechanisms of cyclic deformation, including (i) decrease in overall dislocation density, (ii) loss of low angle boundary dislocations and (iii) a coarsening of the lath microstructure and precipitates. The model captures the experimentally observed phenomena across a range of strain-rates and strain-ranges.
- Hardening effects, produced by the main strengthening mechanisms in 9-12Cr steels, are modelled through the inclusion of evolution equations defining dislocation hardening and precipitate strengthening.
- $M_{23}C_6$ precipitates are predicted to dominate in terms of effect on the plastic strain-range and cyclic strength and hence, life, relative to other precipitate types (e.g. MX precipitates).
- At low temperatures, a lath size effect on plastic strain-range was predicted, i.e. a smaller lath width gave a lower plastic strain-range. However, at the higher temperatures, lath growth is accelerated and the model predicts more rapid saturation of lath width and hence, cyclic softening. Thus, the initial lath width is predicted to have no effect on the plastic strain range at 600 °C.

Acknowledgements

This publication has emanated from research conducted with the financial support of Science Foundation Ireland under Grant Number SFI/10/IN.1/I3015. The Author's would like to acknowledge the contributions made by the collaborators of the METCAM project, including Dr. T.P. Farragher of

NUI Galway, Mr. S. Scully of ESB Energy International, Prof. N.P. O'Dowd, Dr. P. Tiernan, and Dr. D. Li of the University of Limerick and Prof. T.H. Hyde, Dr. C.J. Hyde and Prof. W. Sun of the University of Nottingham.

Table 1: Chemical composition of the service aged P91 steel prior to industrial service [36].

Element	C	Mn	Si	N	Cr	Mo	Nb/ Cb	Cu	V	Al	P	Ni
wt%	0.1	0.42	0.26	0.058	8.48	0.94	0.073	-	0.204	0.007	0.013	0.19

Table 2: Identified temperature-dependent elasto-viscoplastic material parameters.

T (°C)	E (GPa)	$\sigma_{y,0}$ (MPa)	ν	α (/s)	β (/MPa)
400	180	255	0.3	8.0×10^{-6}	0.05
500	165	228	0.3	4.0×10^{-6}	0.05
600	142	196	0.3	4.2×10^{-5}	0.05

Table 3: Temperature-independent microstructural material constants.

Parameter	Value	Parameter	Value
α_1	0.235	$k_{\text{sol}}^{[21]}$	0.05
α_2	3.0	$Q_{\text{CR}}^{[68]}$	400 kJ/mol
$D_{\text{Fe},0}^{[69]}$	$1.6 \times 10^{-4} \text{ m}^2/\text{s}$	$Q_{\delta}^{[42]}$	303 kJ/mol
$d_e^{[14]}$	$6b$	$r_{\text{M23C6}}^{[41]}$	45.0 nm
$\delta_0^{[15]}$	$0.7 \mu\text{m}$	$r_{\text{NbC}}^{[41]}$	25.0 nm
$f_{\text{M23C6}}^{[53]}$	0.019	$r_{\text{VN}}^{[41]}$	20.0 nm
$f_{\text{NbC}}^{[53]}$	0.001	$\rho_{i,0}^{[21]}$	$1.0 \times 10^{11} \text{ mm}^{-2}$
$f_{\text{VN}}^{[53]}$	0.004	$t_w^{[21]}$	$100 b$

Table 4: Identified temperature-independent microstructural parameters.

Parameter	Value	Parameter	Value
$\alpha_{\delta,0}$	1.0×10^{-18}	γ_{δ}	2.002
β_{δ}	2.05×10^{-9}	κ	1.45
d_{dip}	$7b$	ρ_0	$4.5 \times 10^{14} \text{ mm}^{-2}$
d_{lock}	b	$\rho_{w,0}$	$0.9 \rho_0$

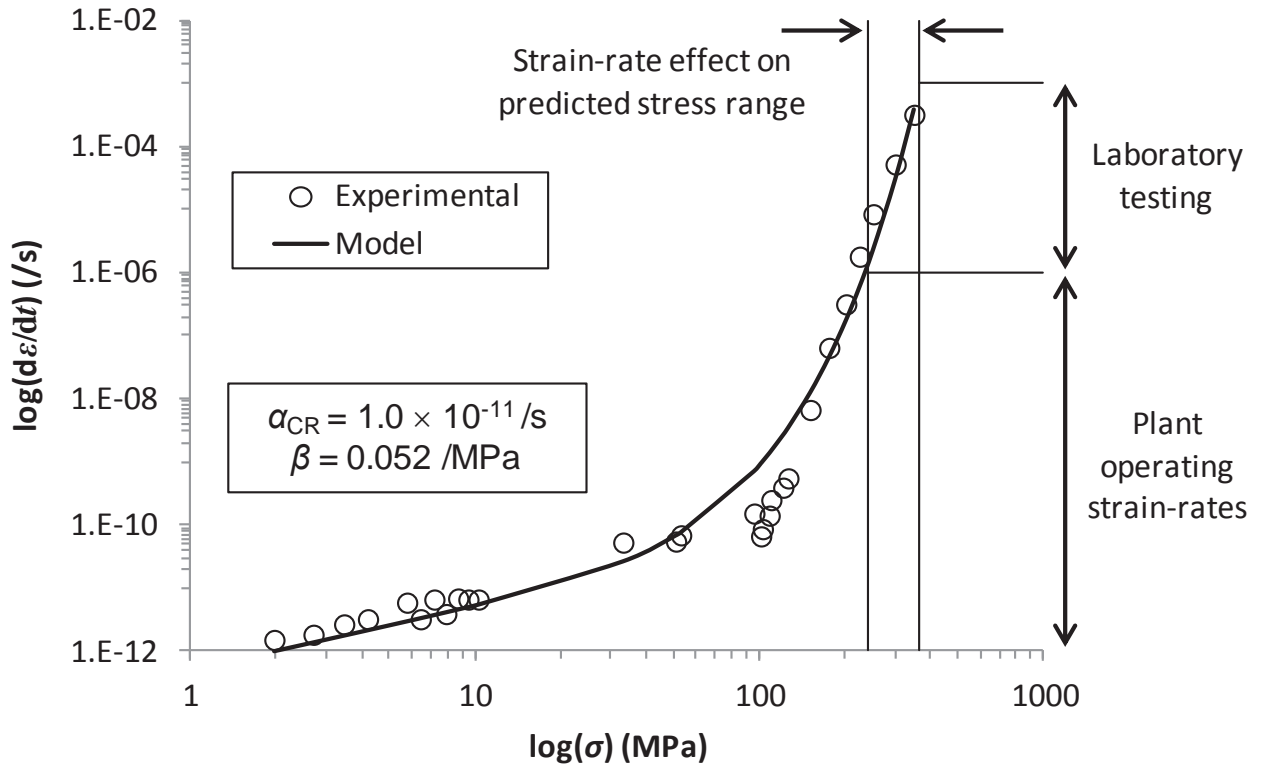


Figure 1: Comparison of the hyperbolic sine model with the experimental data of [70], illustrating the extrapolation capability of the hyperbolic sine formulation at a temperature of 600 °C.

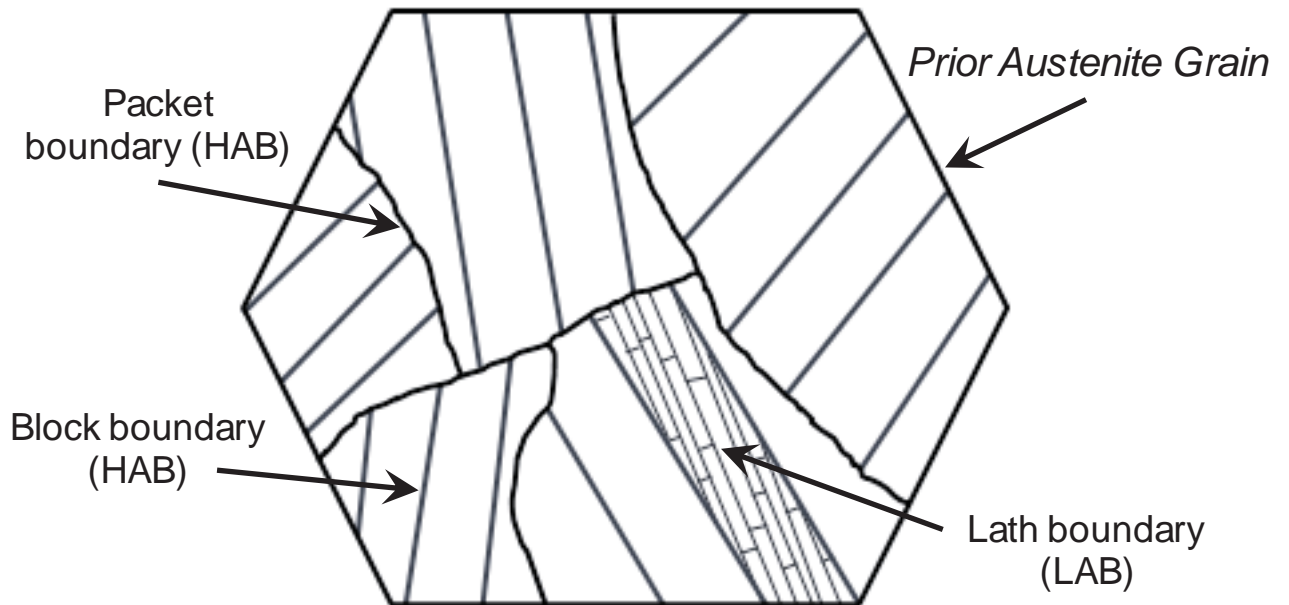


Figure 2: Hierarchical microstructure of 9-12Cr steels.

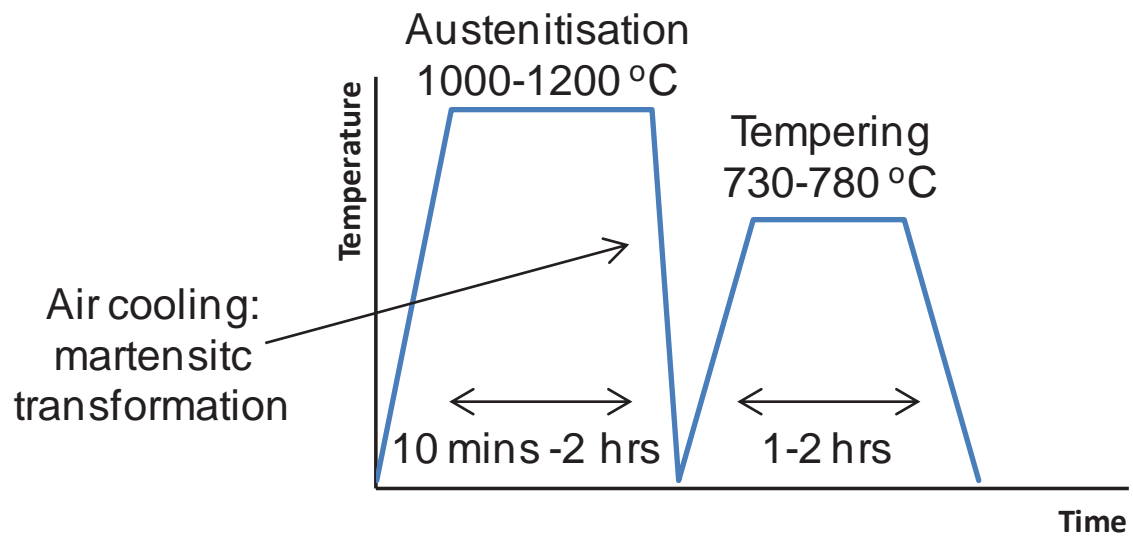


Figure 3: Heat treatment process for 9-12Cr steels.

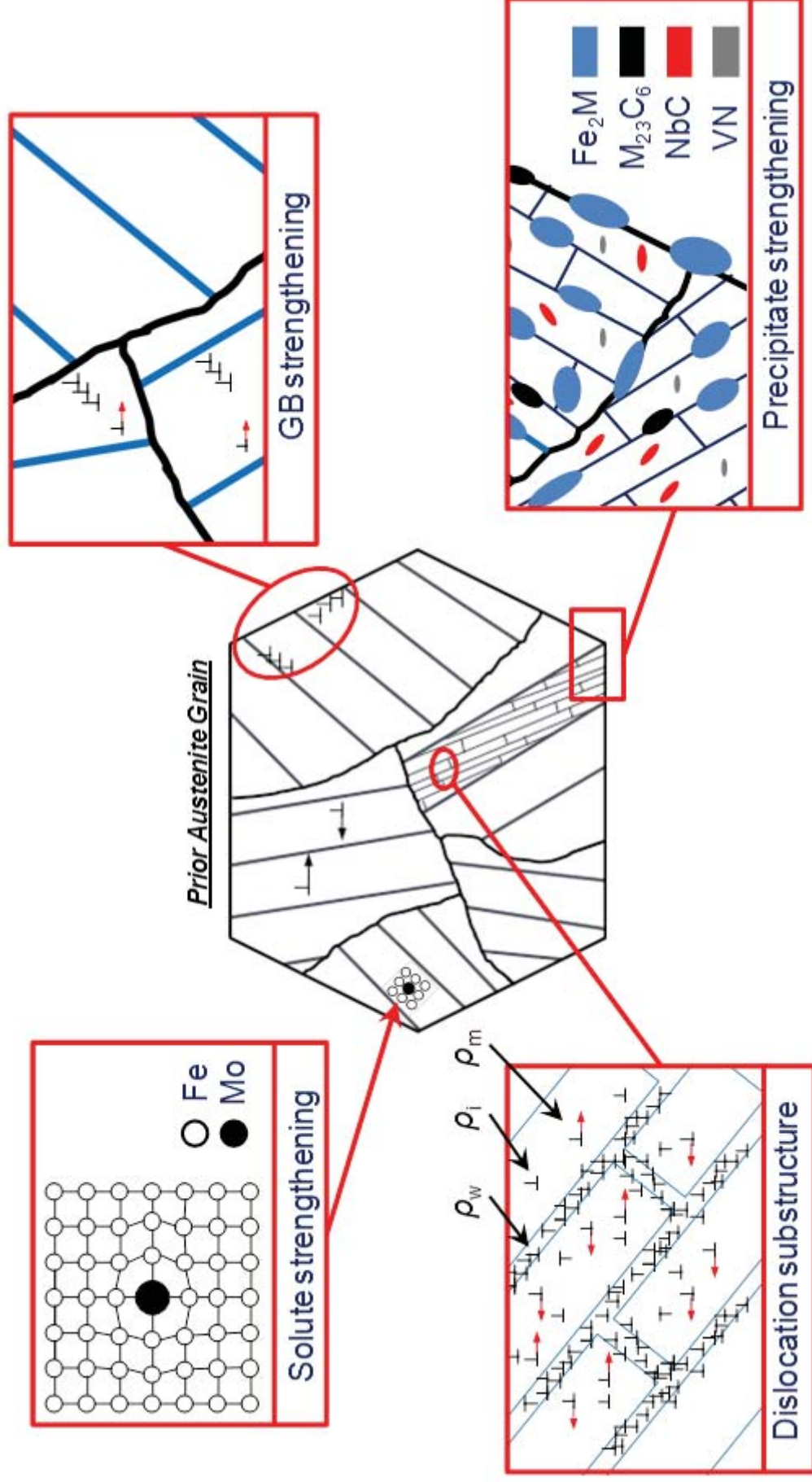


Figure 4: Various strengthening mechanisms in 9-12Cr steels.

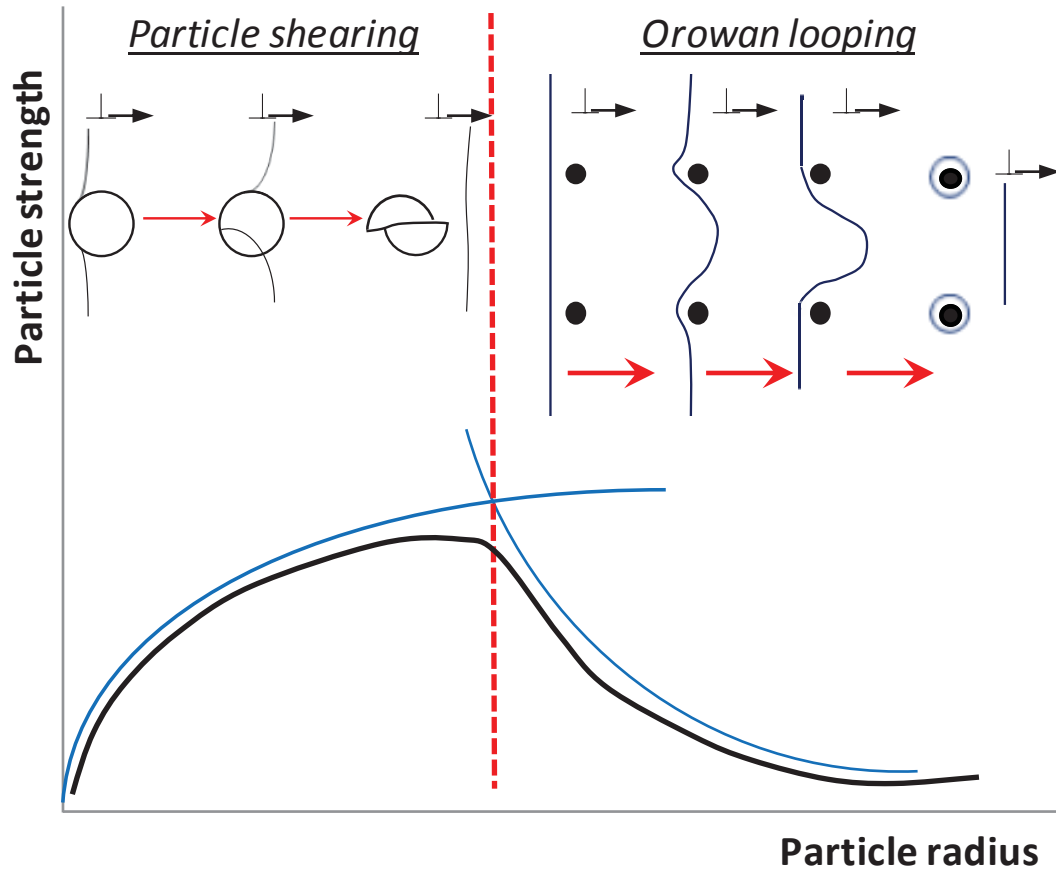


Figure 5: Schematic representation of a dislocation interacting with precipitates in the form of particle shearing and the production of Orowan loops.

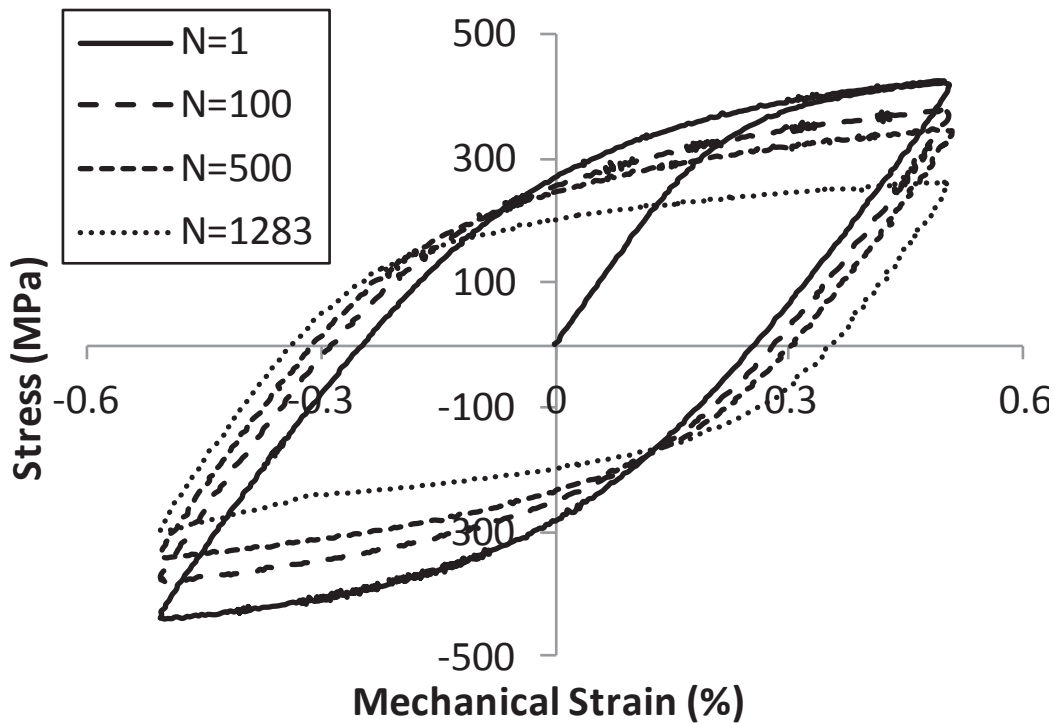


Figure 6: Stress-strain response at a temperature of 500 °C and strain-rate of 0.1 %/s illustrating the cyclic softening behaviour of 9-12Cr steels.

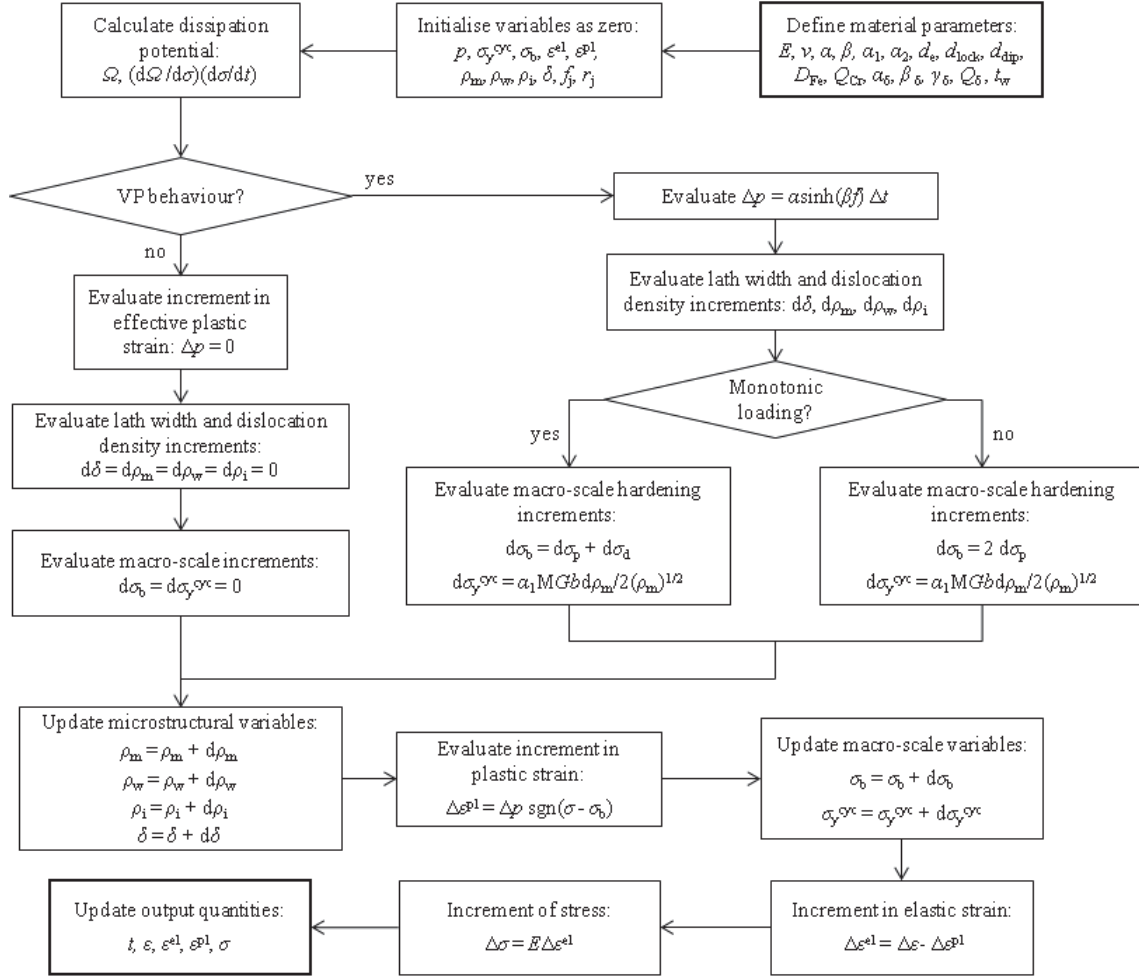


Figure 7: Flowchart of the main processes in the uniaxial material model

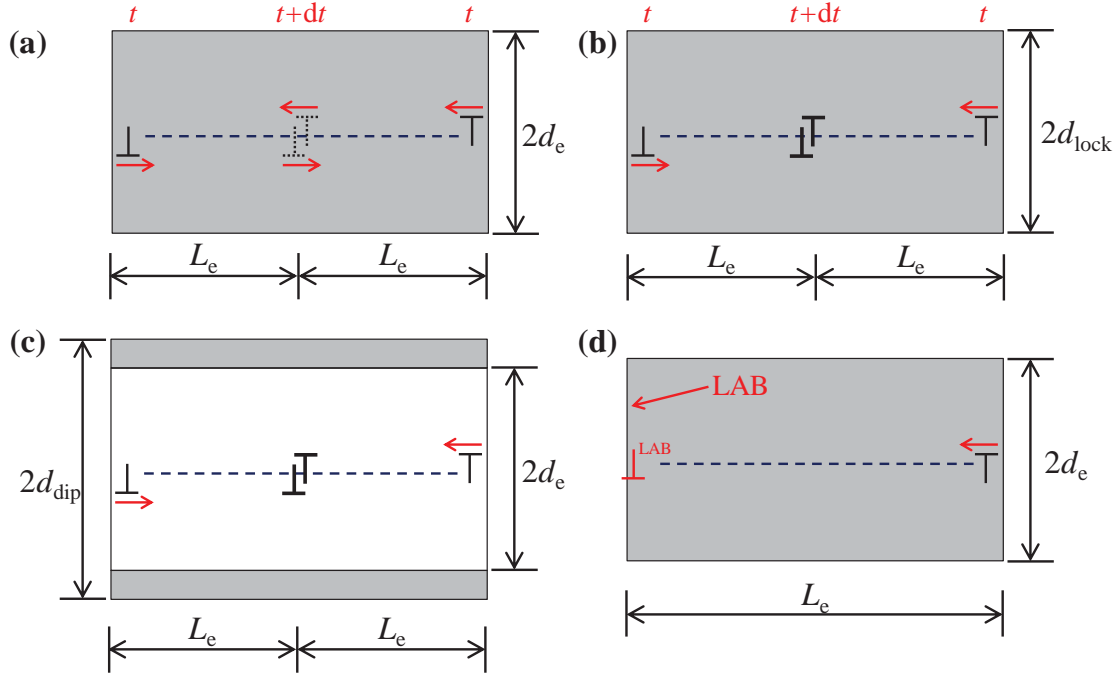


Figure 8: Critical areas (shaded regions) for (a) mutual annihilation of two mobile dislocations, (b) formation of an immobile locked configuration, (c) formation of a dipole configuration and (d) LAB dislocation annihilation.

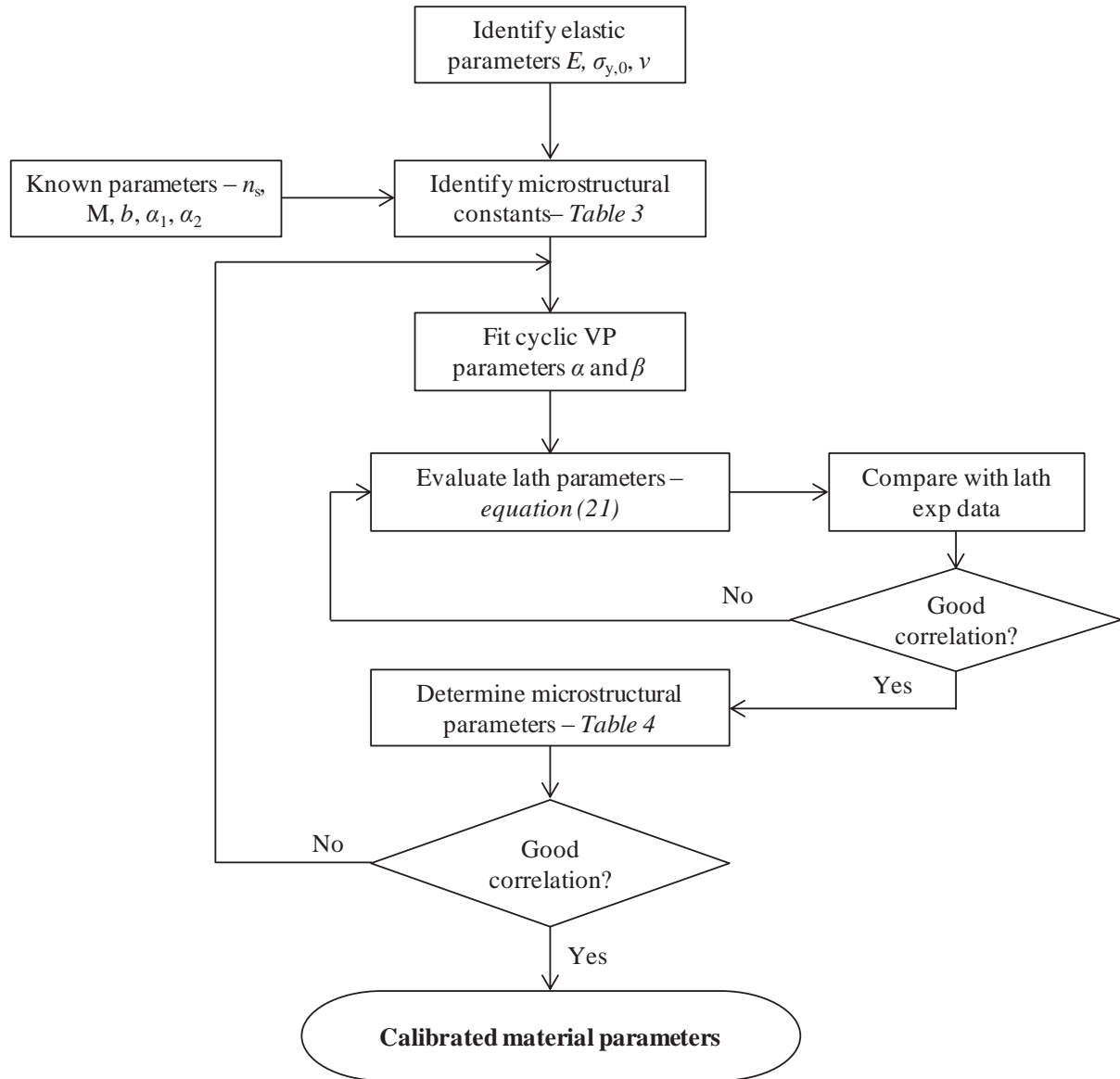


Figure 9: Flowchart for parameter identification method used in the present study.

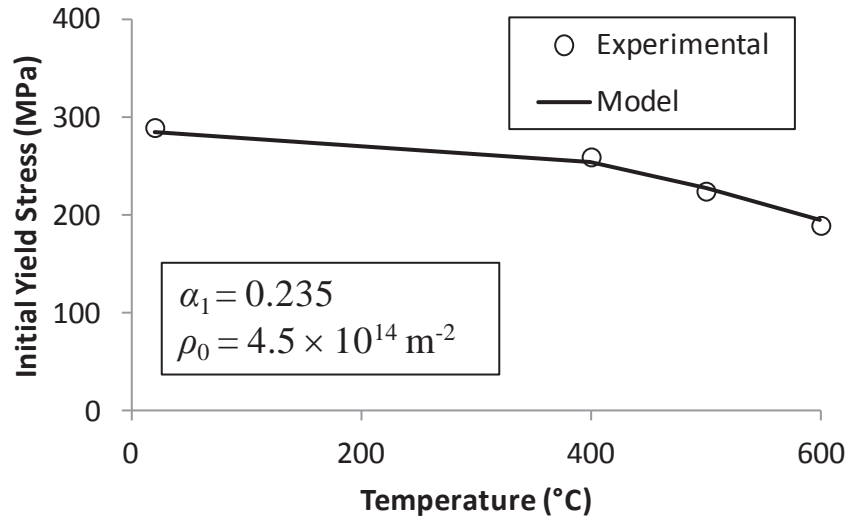


Figure 10: Comparison of the model predicted initial yield stress and the experimental values for various temperatures.

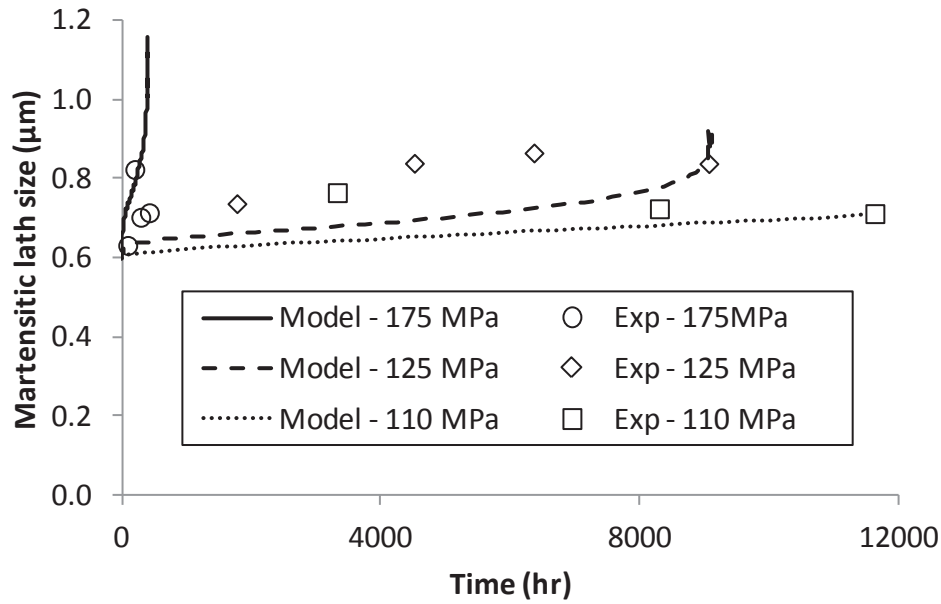
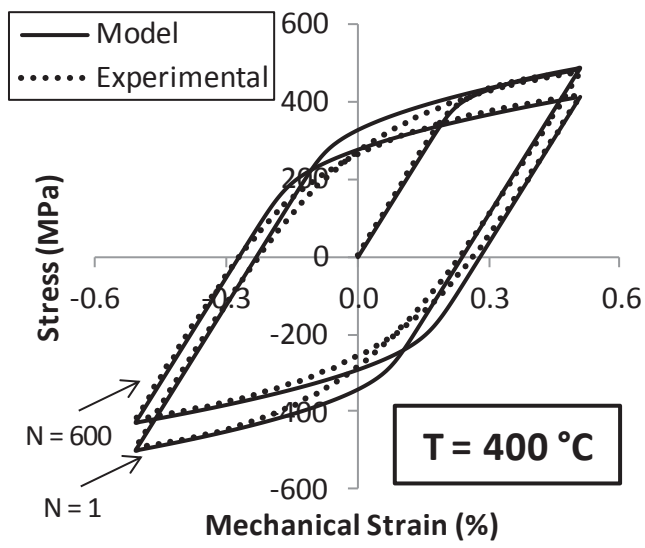
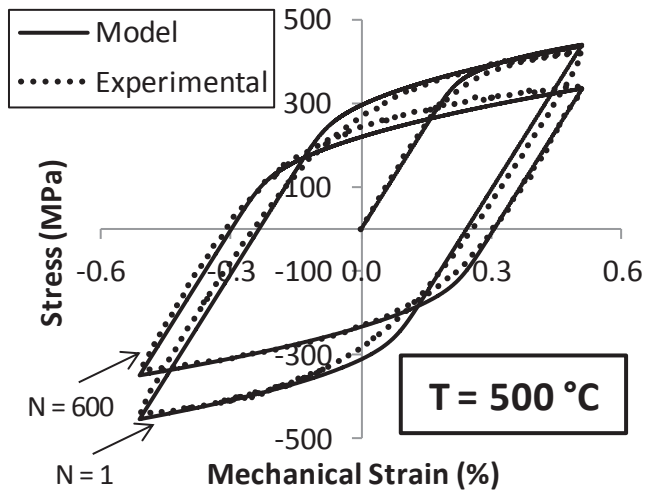


Figure 11: Identification of the martensitic lath growth material parameters from the material data of [57].

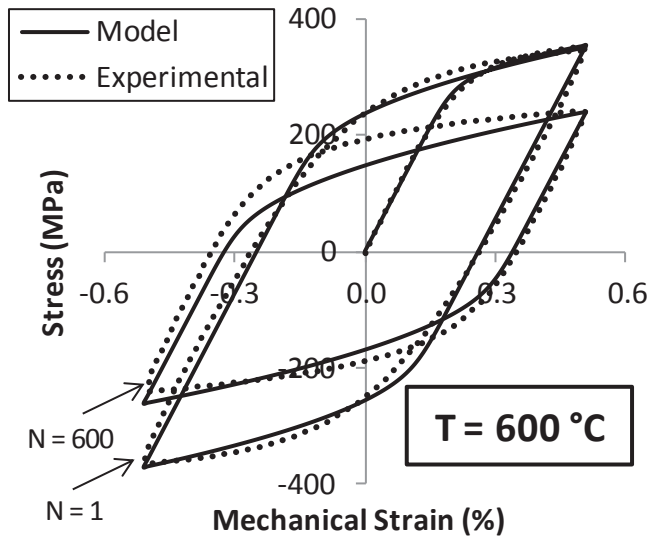
(a)



(b)



(c)



(d)

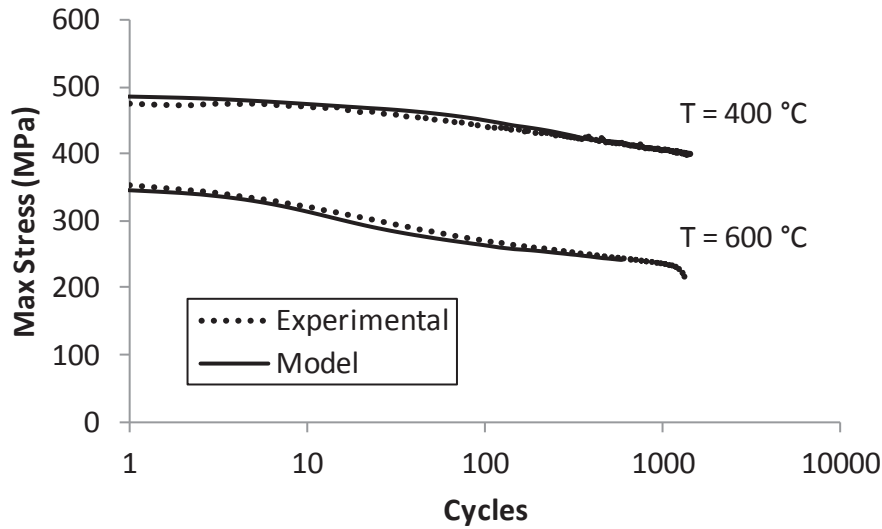
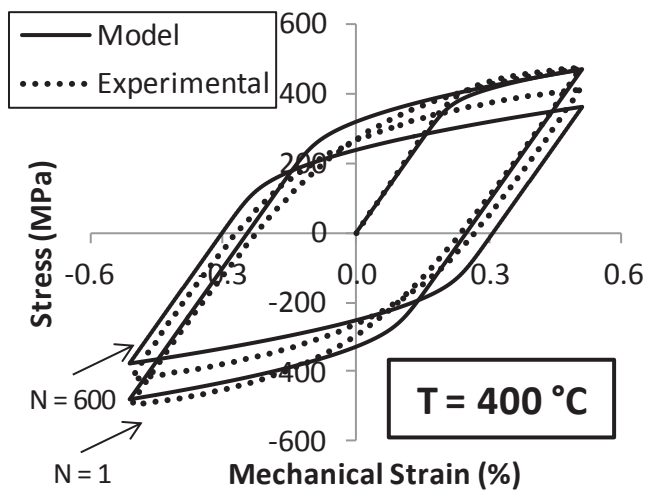
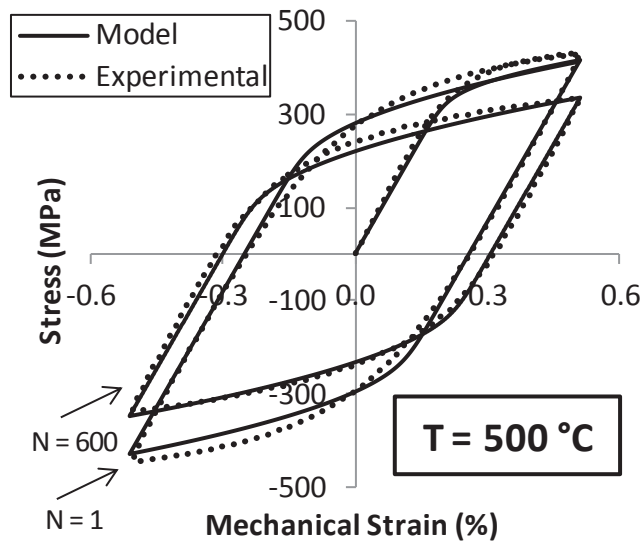


Figure 12: Comparison of calibrated model against measured stress-strain response for the 1st and 600th cycles at a strain-rate of 0.1 %/s and temperature of (a) 400 °C, (b) 500 °C and (c) 600 °C and (d) the evolution of maximum stress with cycles for temperatures of 400 °C and 600 °C.

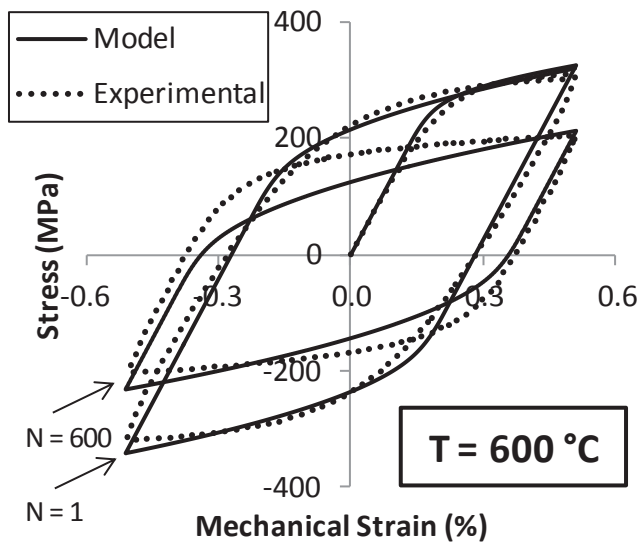
(a)



(b)



(c)



(d)

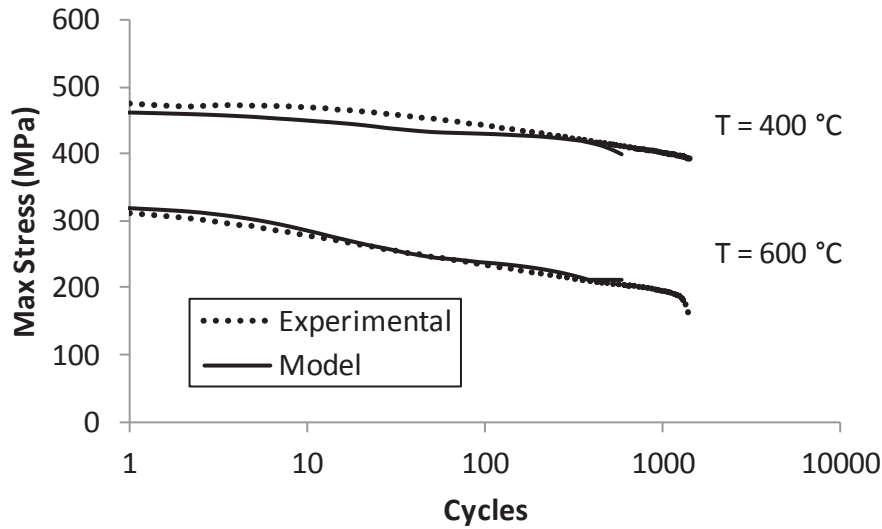
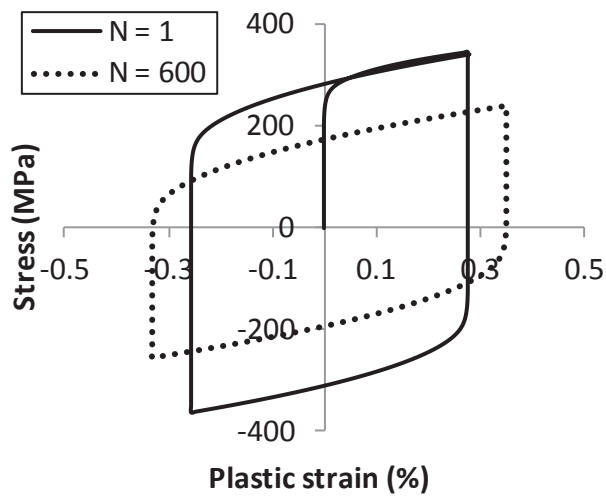


Figure 13: Validation of the material model against measured stress-strain response for the 1st and 600th cycles at a strain-rate of 0.025 %/s and temperature of (a) 400 °C, (b) 500 °C and (c) 600 °C and (d) the evolution of maximum stress with cycles for temperatures of 400 °C and 600 °C.

(a)



(b)

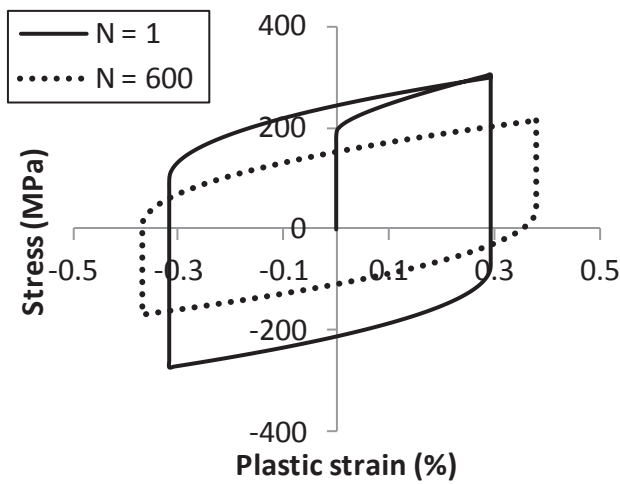


Figure 14: Model prediction of the stress-strain response at 600 °C at strain-rates of (a) 0.1 %/s and (b) 0.0001 %/s.

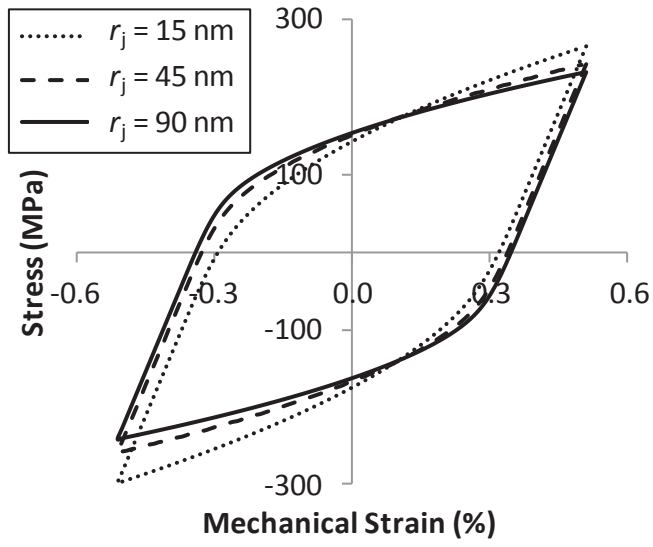
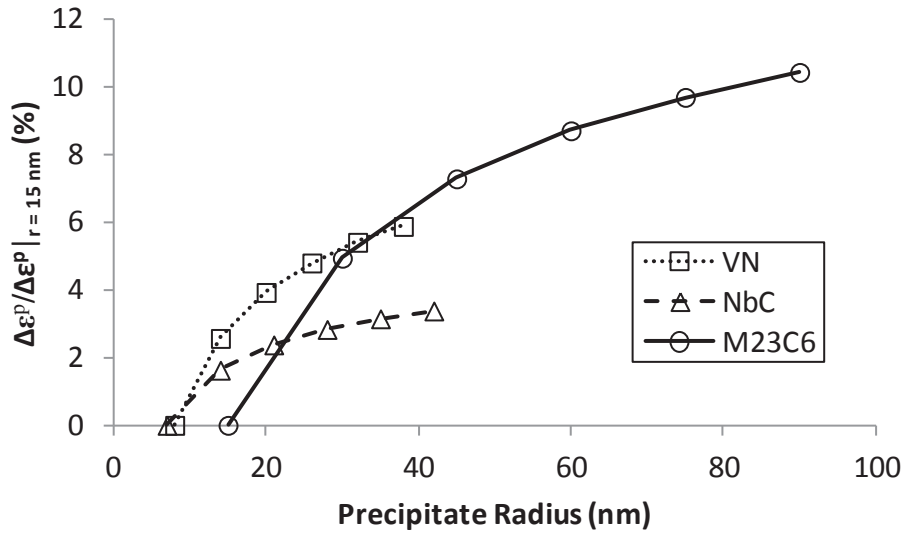


Figure 15: Predicted effect of $M_{23}C_6$ particle radius (r_j) on stress-strain response at 600 °C for a strain-rate of 0.1 %/s for the 600th cycle.

(a)



(b)

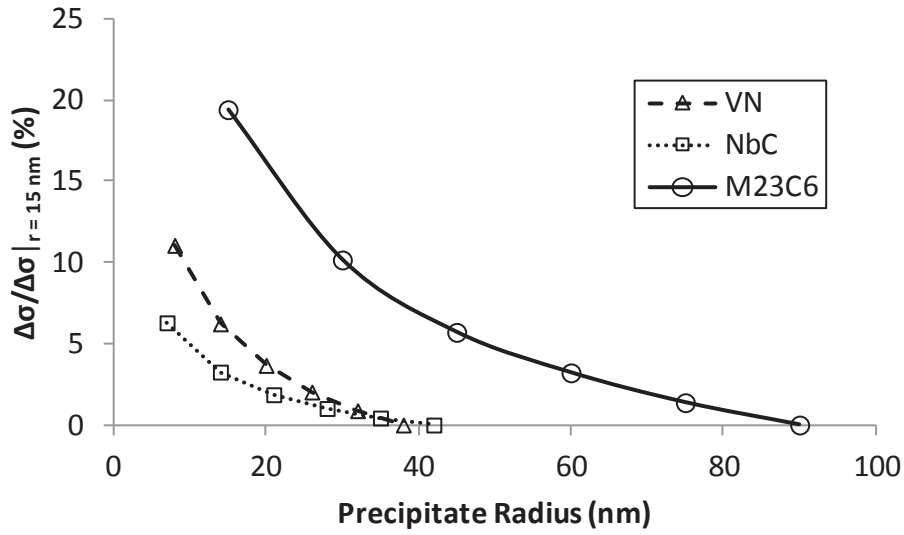


Figure 16: Predicted effect of varying the mean initial precipitate radius of the MX and $M_{23}C_6$ particles (relative to the values at a radius of 15 nm) on (a) the plastic strain range and (b) the stress range at a temperature of 600 °C, strain-range of $\pm 0.5\%$ and a strain-rate of 0.1 %/s.

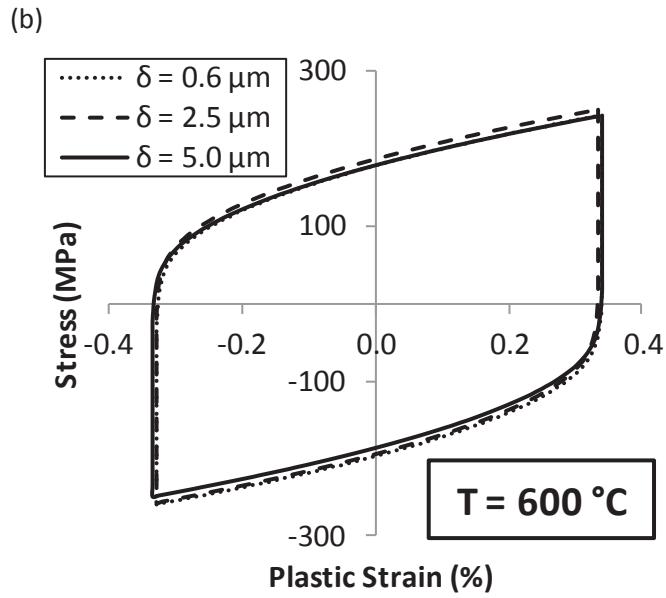
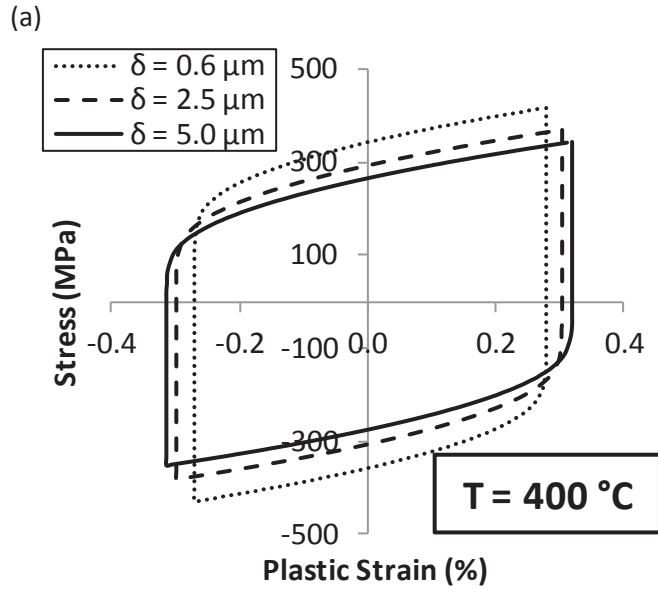


Figure 17: Comparison of the predicted stress-strain responses for various initial martensitic lath sizes at (a) $400\text{ }^{\circ}\text{C}$ and (b) $600\text{ }^{\circ}\text{C}$ for a strain-range of $\pm 0.5\%$ and a strain-rate of $0.1\text{ }\%/s$ for the 600^{th} cycle.

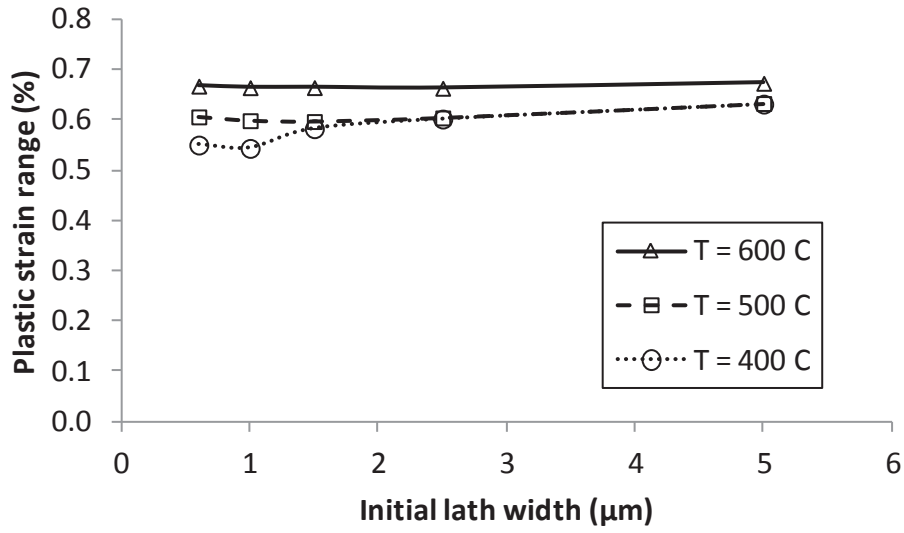
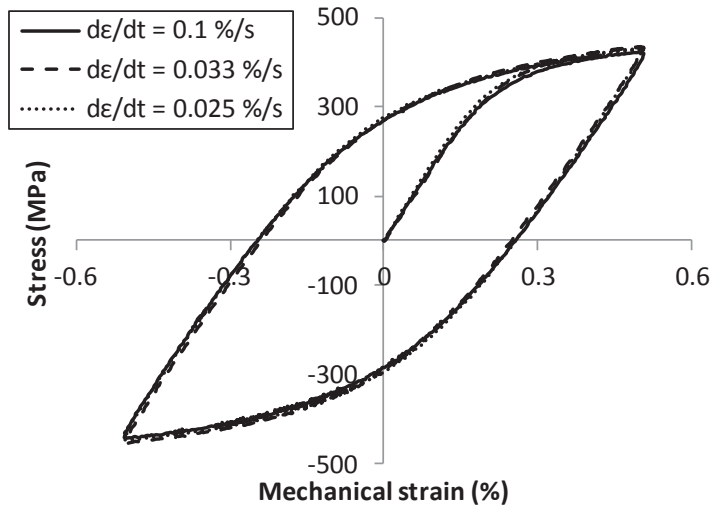


Figure 18: Predicted effect of various the initial mean martensitic lath dimensions on the plastic strain-range produced for 400 °C, 500 °C and 600 °C for the 600th cycle.

(a)



(b)

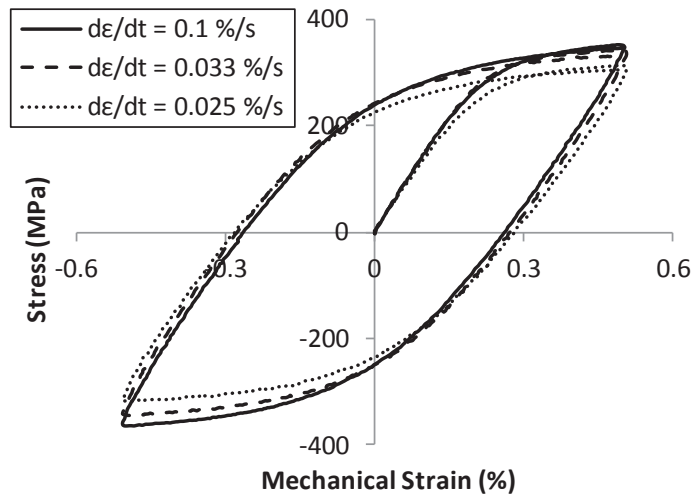


Figure 19: Strain-rate effect observed in cyclic plasticity experiments for the initial cycle at (a) 500 °C and (b) 600 °C.

References

- [1] T.P. Farragher, S. Scully, N.P. O'Dowd, S.B. Leen, Thermomechanical Analysis of a Pressurized Pipe Under Plant Conditions, *Journal of Pressure Vessel Technology*, 135 (2013) 011204-011209.
- [2] T.P. Farragher, S. Scully, N.P. O'Dowd, S.B. Leen, Development of life assessment procedures for power plant headers operated under flexible loading scenarios, *International Journal of Fatigue*, 49 (2013) 50-61.
- [3] S. Scully, ESB Energy International, Personal Communication, 2012.
- [4] J. Zachary, P. Kochis, R. Narula, Steam turbine design considerations for supercritical cycles, *Coal Gen*, Milwaukee, WI, 2007.
- [5] F. Abe, M. Taneike, K. Sawada, Alloy design of creep resistant 9Cr steel using a dispersion of nano-sized carbonitrides, *International Journal of Pressure Vessels and Piping*, 84 (2007) 3-12.
- [6] C.G. Panait, A. Zielińska-Lipiec, T. Koziel, A. Czyrska-Filemonowicz, A.-F. Gourgues-Lorenzon, W. Bendick, Evolution of dislocation density, size of subgrains and MX-type precipitates in a P91 steel during creep and during thermal ageing at 600 °C for more than 100,000 h, *Materials Science and Engineering: A*, 527 (2010) 4062-4069.
- [7] J.L. Chaboche, G. Rousselier, On the Plastic and Viscoplastic Constitutive Equations-Part I: Rules Developed With Internal Variable Concept, *Journal of Pressure Vessel Technology*, 105 (1983) 153-158.
- [8] J.L. Chaboche, G. Rousselier, On the Plastic and Viscoplastic Constitutive Equations-Part II: Application of Internal Variable Concepts to the 316 Stainless Steel, *Journal of Pressure Vessel Technology*, 105 (1983) 159-164.
- [9] C.J. Hyde, W. Sun, S.B. Leen, Cyclic thermo-mechanical material modelling and testing of 316 stainless steel, *International Journal of Pressure Vessels and Piping*, 87 (2010) 365-372.
- [10] A.A. Saad, W. Sun, T.H. Hyde, D.W.J. Tanner, Cyclic softening behaviour of a P91 steel under low cycle fatigue at high temperature, *Procedia Engineering*, 10 (2011) 1103-1108.
- [11] R.A. Barrett, P.E. O'Donoghue, S.B. Leen, An improved unified viscoplastic constitutive model for strain-rate sensitivity in high temperature fatigue, *International Journal of Fatigue*, 48 (2013) 192-204.
- [12] R.A. Barrett, T.P. Farragher, C.J. Hyde, N.P. O'Dowd, P.E. O'Donoghue, S.B. Leen, A Unified Viscoplastic Model for High Temperature Low Cycle Fatigue of Service-Aged P91 Steel, *Journal of Pressure Vessel Technology*, 136 (2014) 021402-021402.
- [13] R.A. Barrett, T.P. Farragher, N.P. O'Dowd, P.E. O'Donoghue, S.B. Leen, Multiaxial cyclic viscoplasticity model for high temperature fatigue of P91 steel, *Materials Science and Technology*, 30 (2014) 67-74.
- [14] M. Sauzay, H. Brillet, I. Monnet, M. Mottot, F. Barcelo, B. Fournier, A. Pineau, Cyclically induced softening due to low-angle boundary annihilation in a martensitic steel, *Materials Science and Engineering: A*, 400-401 (2005) 241-244.
- [15] M. Sauzay, B. Fournier, M. Mottot, A. Pineau, I. Monnet, Cyclic softening of martensitic steels at high temperature—Experiments and physically based modelling, *Materials Science and Engineering: A*, 483-484 (2008) 410-414.
- [16] A. Ma, F. Roters, D. Raabe, A dislocation density based constitutive law for BCC materials in crystal plasticity FEM, *Computational Materials Science*, 39 (2007) 91-95.
- [17] F. Roters, D. Raabe, G. Gottstein, Work hardening in heterogeneous alloys—a microstructural approach based on three internal state variables, *Acta Materialia*, 48 (2000) 4181-4189.
- [18] E. Hosseini, M. Kazeminezhad, A new microstructural model based on dislocation generation and consumption mechanisms through severe plastic deformation, *Computational Materials Science*, 50 (2011) 1123-1135.
- [19] E. Nes, Modelling of work hardening and stress saturation in FCC metals, *Progress in Materials Science*, 41 (1997) 129-193.
- [20] L. Esposito, N. Bonora, A primary creep model for Class M materials, *Materials Science and Engineering: A*, 528 (2011) 5496-5501.

- [21] H. Magnusson, R. Sandström, Creep Strain Modeling of 9 to 12 Pct Cr Steels Based on Microstructure Evolution, *Metallurgical and Materials Transactions A*, 38 (2007) 2033-2039.
- [22] H. Magnusson, R. Sandström, The Role of Dislocation Climb across Particles at Creep Conditions in 9 to 12 Pct Cr Steels, *Metallurgical and Materials Transactions A*, 38 (2007) 2428-2434.
- [23] S. Spigarelli, E. Quadri, Analysis of the creep behaviour of modified P91 (9Cr–1Mo–NbV) welds, *Materials & Design*, 23 (2002) 547-552.
- [24] S. Spigarelli, Microstructure-based assessment of creep rupture strength in 9Cr steels, *International Journal of Pressure Vessels and Piping*, 101 (2013) 64-71.
- [25] S. Spigarelli, Quantification of the effect of early microstructural degradation during creep of 9Cr–1Mo–NbV steels at 600 °C, *Materials Science and Engineering: A*, 565 (2013) 269-277.
- [26] A. Orlová, Subgrain size in view of the composite model of dislocation structure, *Materials Science and Engineering: A*, 297 (2001) 281-285.
- [27] E.M. Viatkina, W.A.M. Brekelmans, M.G.D. Geers, Modelling the evolution of dislocation structures upon stress reversal, *International Journal of Solids and Structures*, 44 (2007) 6030-6054.
- [28] K.-S. Cheong, E.P. Busso, Discrete dislocation density modelling of single phase FCC polycrystal aggregates, *Acta Materialia*, 52 (2004) 5665-5675.
- [29] K.S. Cheong, E.P. Busso, A. Arsenlis, A study of microstructural length scale effects on the behaviour of FCC polycrystals using strain gradient concepts, *International Journal of Plasticity*, 21 (2005) 1797-1814.
- [30] C.J. Bayley, W.A.M. Brekelmans, M.G.D. Geers, A comparison of dislocation induced back stress formulations in strain gradient crystal plasticity, *International Journal of Solids and Structures*, 43 (2006) 7268-7286.
- [31] L.P. Evers, W.A.M. Brekelmans, M.G.D. Geers, Scale dependent crystal plasticity framework with dislocation density and grain boundary effects, *International Journal of Solids and Structures*, 41 (2004) 5209-5230.
- [32] C.A. Sweeney, W. Vorster, S.B. Leen, E. Sakurada, P.E. McHugh, F.P.E. Dunne, The role of elastic anisotropy, length scale and crystallographic slip in fatigue crack nucleation, *Journal of the Mechanics and Physics of Solids*, 61 (2013) 1224-1240.
- [33] B. Fournier, M. Sauzay, M. Mottot, H. Brillet, I. Monnet, A. Pineau, Experimentally based modelling of cyclically induced softening in a martensitic steel at high temperature, *ECCC Creep Conference*, London, UK, 2005.
- [34] F. Abe, M. Tabuchi, S. Tsukamoto, T. Shirane, Microstructure evolution in HAZ and suppression of Type IV fracture in advanced ferritic power plant steels, *International Journal of Pressure Vessels and Piping*, 87 (2010) 598-604.
- [35] W. Yan, W. Wang, Y.-Y. Shan, K. Yang, Microstructural stability of 9–12%Cr ferrite/martensite heat-resistant steels, *Frontiers of Materials Science*, 7 (2013) 1-27.
- [36] T.P. Farragher, C.J. Hyde, W. Sun, T.H. Hyde, N.P. O'Dowd, S. Scully, S.B. Leen, High temperature low cycle fatigue behaviour of service-aged P91 material, 9th International Conference on Creep and Fatigue at Elevated Temperatures, IOM3, London, UK, 2012.
- [37] F. Abe, T. Horiuchi, M. Taneike, K. Sawada, Stabilization of martensitic microstructure in advanced 9Cr steel during creep at high temperature, *Materials Science and Engineering: A*, 378 (2004) 299-303.
- [38] C.G. Panait, W. Bendick, A. Fuchsmann, A.F. Gourgues-Lorenzon, J. Besson, Study of the microstructure of the Grade 91 steel after more than 100,000 h of creep exposure at 600 °C, *International Journal of Pressure Vessels and Piping*, 87 (2010) 326-335.
- [39] F. Abe, Precipitate design for creep strengthening of 9% Cr tempered martensitic steel for ultra-supercritical power plants, *Science and Technology of Advanced Materials*, 9 (2008) 013002.
- [40] P.J. Ennis, A. Zielinska-Lipiec, O. Wachter, A. Czyrska-Filemonowicz, Microstructural stability and creep rupture strength of the martensitic steel P92 for advanced power plant, *Acta Materialia*, 45 (1997) 4901-4907.

- [41] K. Maruyama, K. Sawada, J.-i. Koike, Strengthening Mechanisms of Creep Resistant Tempered Martensitic Steel, *ISIJ International*, 41 (2001) 641-653.
- [42] R. Oruganti, M. Karadge, S. Swaminathan, Damage mechanics-based creep model for 9–10%Cr ferritic steels, *Acta Materialia*, 59 (2011) 2145-2155.
- [43] F. Vakili-Tahami, D.R. Hayhurst, M.T. Wong, High-Temperature Creep Rupture of Low Alloy Ferritic Steel Butt-Welded Pipes Subjected to Combined Internal Pressure and End Loadings, *Philosophical Transactions: Mathematical, Physical and Engineering Sciences*, 363 (2005) 2629-2661.
- [44] S. Suresh, *Fatigue of materials*, Cambridge : Cambridge University Press, Cambridge, 1998.
- [45] L.A. Gypen, A. Deruyttere, Multi-component solid solution hardening, *Journal of Materials Science*, 12 (1977) 1028-1033.
- [46] L.A. Gypen, A. Deruyttere, Multi-component solid solution hardening, *Journal of Materials Science*, 12 (1977) 1034-1038.
- [47] J.C. Fisher, E.W. Hart, R.H. Pry, The hardening of metal crystals by precipitate particles, *Acta Metallurgica*, 1 (1953) 336-339.
- [48] E.W. Hart, Theory of dispersion hardening in metals, *Acta Metallurgica*, 20 (1972) 275-289.
- [49] O. Ryen, *Work Hardening and Mechanical Anisotropy of Aluminium Sheets and Profiles*, Ph.D Thesis, The Norwegian University of Science and Technology (NTNU), 2003.
- [50] E. Orowan, Problems of plastic gliding, *Philosophical Transactions of the Royal Society of London, A*, 52 (1940) 8-22.
- [51] G.I. Taylor, Plastic Strain in Metals, *Journal of the Institute of Metals*, 62 (1938) 307-324.
- [52] J. Lin, F.P.E. Dunne, Modelling grain growth evolution and necking in superplastic blow-forming, *International Journal of Mechanical Sciences*, 43 (2001) 595-609.
- [53] B.S. Srinivas Prasad, V.B. Rajkumar, K.C. Hari Kumar, Numerical simulation of precipitate evolution in ferritic–martensitic power plant steels, *Calphad*, 36 (2012) 1-7.
- [54] P.J. Ennis, A. Czyrska-Filemonowicz, Recent advances in creep-resistant steels for power plant applications, *Sadhana*, 28 (2003) 709-730.
- [55] J. Pešička, R. Kužel, A. Dronhofer, G. Eggeler, The evolution of dislocation density during heat treatment and creep of tempered martensite ferritic steels, *Acta Materialia*, 51 (2003) 4847-4862.
- [56] L. Collini, A. Bonardi, A micromechanical model of the evolution of stress and strain fields in ultrafine-grained metal structures under tension, *The Journal of Strain Analysis for Engineering Design*, 48 (2013) 91-102.
- [57] A. Orlová, J. Buršík, K. Kuchařová, V. Sklenička, Microstructural development during high temperature creep of 9% Cr steel, *Materials Science and Engineering: A*, 245 (1998) 39-48.
- [58] F. Nabarro, Creep at very low rates, *Metallurgical and Materials Transactions A*, 33 (2002) 213-218.
- [59] A. Kostka, K.G. Tak, R.J. Hellmig, Y. Estrin, G. Eggeler, On the contribution of carbides and micrograin boundaries to the creep strength of tempered martensite ferritic steels, *Acta Materialia*, 55 (2007) 539-550.
- [60] M.E. Kassner, Role of small-angle (subgrain boundary) and large-angle (grain boundary) interfaces on 5- and 3-power-law creep, *Materials Science and Engineering: A*, 166 (1993) 81-88.
- [61] R.D. Doherty, D.A. Hughes, F.J. Humphreys, J.J. Jonas, D.J. Jensen, M.E. Kassner, W.E. King, T.R. McNelley, H.J. McQueen, A.D. Rollett, Current issues in recrystallization: a review, *Materials Science and Engineering: A*, 238 (1997) 219-274.
- [62] M.E. Kassner, Taylor hardening in five-power-law creep of metals and Class M alloys, *Acta Materialia*, 52 (2004) 1-9.
- [63] B.J. Golden, D.F. Li, N.P. O'Dowd, P. Tiernan, Microstructural Modeling of P91 Martensitic Steel Under Uniaxial Loading Conditions, *Journal of Pressure Vessel Technology*, 136 (2014) 021404-021404.
- [64] D.-F. Li, Golden, B.J., O'Dowd, N.P., Modelling of micro-plasticity evolution in crystalline materials, in: *ASME Pressure Vessels and Piping Division Conference*, 2013, ASME, Paris, France, 2013.

- [65] C.A. Sweeney, B. O'Brien, P.E. McHugh, S.B. Leen, Experimental characterisation for micromechanical modelling of CoCr stent fatigue, *Biomaterials*, 35 (2014) 36-48.
- [66] A. Manonukul, F.P.E. Dunne, High- and low-cycle fatigue crack initiation using polycrystal plasticity, *Proceedings of the Royal Society of London. Series A: Mathematical, Physical and Engineering Sciences*, 460 (2004) 1881-1903.
- [67] M.D. Sangid, H.J. Maier, H. Sehitoglu, A physically based fatigue model for prediction of crack initiation from persistent slip bands in polycrystals, *Acta Materialia*, 59 (2011) 328-341.
- [68] D. Samantaray, C. Phaniraj, S. Mandal, A.K. Bhaduri, Strain dependent rate equation to predict elevated temperature flow behavior of modified 9Cr-1Mo (P91) steel, *Materials Science and Engineering: A*, 528 (2011) 1071-1077.
- [69] M.F. Ashby, D.R. Jones, *Engineering materials 1 : an introduction to properties, applications and design*, Boston : Elsevier Butterworth-Heinemann, 2005.
- [70] V. Sklenička, K. Kuchařová, M. Svoboda, L. Kloc, Burší, amp, x, J. k, A. Kroupa, Long-term creep behavior of 9–12%Cr power plant steels, *Materials Characterization*, 51 (2003) 35-48.